

Morphological properties of $z \sim 0.5$ absorption-selected galaxies: the role of galaxy inclination

Glenn G. Kacprzak,^{1*} Christopher W. Churchill,² Jessica L. Evans,² Michael T. Murphy,¹ and Charles C. Steidel³

¹ Centre for Astrophysics and Supercomputing, Swinburne University of Technology, PO Box 218, Victoria 3122, Australia

² Department of Astronomy, New Mexico State University, Las Cruces, NM 88003

³ California Institute of Technology, MS 105-24, Pasadena, CA 91125, USA

Accepted June 15, 2011

ABSTRACT

We have used GIM2D to quantify the morphological properties of 40 intermediate redshift MgII absorption-selected galaxies ($0.03 \leq W_r(2796) \leq 2.9 \text{ \AA}$), imaged with WFPC-2/*HST*, and compared them to the halo gas properties measured from HIRES/Keck and UVES/VLT quasar spectra. We find that as the quasar–galaxy separation, D , increases the MgII equivalent decreases with large scatter, implying that D is not the only physical parameter affecting the distribution and quantity of halo gas. Our main result shows that inclination correlates with MgII absorption properties after normalizing out the relationship (and scatter) between the absorption properties and D . We find a 4.3σ correlation between $W_r(2796)$ and galaxy inclination, normalized by impact parameter, i/D . Other measures of absorption optical depth also correlate with i/D at greater than 3.2σ significance. Overall, this result suggests that MgII gas has a co-planar geometry, not necessarily disk-like, that is coupled to the galaxy inclination. It is plausible that the absorbing gas arises from tidal streams, satellites, filaments, etc., which tend to have somewhat co-planar distributions. This result does not support a picture in which MgII absorbers with $W_r(2796) \lesssim 1 \text{ \AA}$ are predominantly produced by star-formation driven winds.

We further find that; (1) MgII host galaxies have quantitatively similar bulge and disk scale length distribution to field galaxies at similar redshifts and have a mean disk and bulge scale length of 3.8 kpc and 2.5 kpc, respectively; (2) Galaxy color and luminosity do not correlate strongly with absorption properties, implying a lack of a connection between host galaxy star formation rates and absorption strength; (3) Parameters such as scale lengths and bulge-to-total ratios do not significantly correlate with the absorption parameters, suggesting that the absorption is independent of galaxy size or mass.

Key words: —galaxies: ISM, haloes —quasars: absorption lines.

1 INTRODUCTION

Since the first observational evidence associating foreground galaxies with absorption lines detected in the spectra of background quasars (Boksenberg & Sargent 1978), researchers have strived to determine the relationships between absorbing gas found within $\sim 200 \text{ km s}^{-1}$ and a few 100 kpc of their host galaxies. We have yet to develop a complete understanding of the many physical conditions under which galaxies predominantly produce their own metal-enriched “halos” or accrete material in their immediate environment. It is plausible that most galaxies undergo both these processes at some point during their evolution. Assuming that clear observational connections between the galaxy properties and the halo

gas properties are present in nature, our collective hope is that we can ultimately understand the conditions that drive outflows versus the conditions that indicate accretion (such as galaxy star formation rates, morphologies, inclinations, etc., and absorption equivalent widths, kinematics, and chemical and ionization conditions).

The MgII $\lambda\lambda 2796, 2803$ doublet is commonly used to trace metal-enriched low-ionized gas surrounding galaxies between $0.1 \leq z \leq 2.5$. However, understanding the origins of this gas is difficult. MgII absorption traces a wide range of neutral hydrogen column densities, $10^{16} \leq N(\text{H I}) \leq 10^{22} \text{ cm}^{-2}$ (Churchill et al. 2000a; Rigby, Charlton, & Churchill 2002), which produces a large range of detectable MgII rest-frame equivalent widths, $0.02 \leq W_r(2796) \leq 10 \text{ \AA}$. The large range in H I column densities implies that MgII absorption arises within a large dynamical range of structures and environments that contribute to the complex kinematics

* gkacprzak@astro.swin.edu.au

seen in typical absorption profiles. It may be that lower column density systems trace a different population of structures and gas producing processes than do higher column density systems.

The first suggestion that halos observed via MgII absorption may exhibit a dependence on galaxy–quasar separation was a $\sim 3\sigma$ anti-correlation between $W_r(2796)$ and impact parameter, D (e.g., Lanzetta & Bowen 1990; Steidel 1995; Churchill et al. 2000b). This could be interpreted to imply the universal property of a radially decreasing gas density profile in halos. However, given the complex velocity structure of these absorption systems, which is independent of D , Churchill, Steidel, & Vogt (1996) argued that the absorption likely arises from a variety of ongoing dynamical events within the galaxy and halo.

The first hint of a connection between galaxy mass and the presence or absence of absorption was deduced from the Holmberg-like luminosity scaling between a characteristic halo radius and galaxy K-band luminosity (Steidel 1995). Recent studies at $0.2 \leq z \leq 1$ restrict the range of the luminosity power-law slope between $0.2 \leq \beta \leq 0.5$, the characteristic MgII halo radius between 90–110 kpc (for an L_B^* galaxy), and the gas absorption covering fraction between ~ 50 – 90% (Tripp & Bowen 2005; Chen & Tinker 2008; Kacprzak et al. 2008; Chen et al. 2010a). However, the MgII gas covering fraction may decrease to $\sim 25\%$ by $z = 0.1$ (Barton & Cooke 2009). It remains unclear what physical processes replenish the gas reservoirs and populate halos with such high covering fractions at high impact parameters.

Bond et al. (2001b) analyzed several systems with $W_r(2796) > 1.8 \text{ \AA}$ at $z > 1$ and concluded that high equivalent width absorption systems produced by winds is a plausible model. Bouché et al. (2006) found an anti-correlation between $W_r(2796)$ and the amplitude of the cross-correlation between luminous red galaxies (LRGs) and MgII absorbers with $W_r(2796) > 1 \text{ \AA}$. Since the cross-correlation amplitude is related to the halo mass, they inferred that the majority of strong absorption systems are *not* produced by gas that is virialized within galaxy halos. They interpreted the $W_r(2796)$ –halo-mass anti-correlation as evidence that supernova-driven winds become dominant sources of stronger MgII absorbers, i.e., $W_r(2796) > 2 \text{ \AA}$. Further support for a wind interpretation of such strong absorbers was found by Zibetti et al. (2007) by stacking Sloan *g*, *r*, and *i* band images toward 700 quasars. Spectral energy distribution fits to their stacked images indicate that early-type galaxies are associated with weaker absorption than late-type galaxies, which suggests that star formation rates (SFRs) may correlate with MgII absorption strength. Confirming these results, Ménard et al. (2009) stacked over 8,500 segments of SDSS quasar spectra where [OII] was likely to be present at the redshift of the MgII absorption and discovered a highly significant correlation between the $W_r(2796)$ and [OII] luminosity. They further demonstrated that the distribution function of $W_r(2796)$ naturally reproduces the shape and amplitude of the [OII] luminosity without any free parameters. This implies that MgII absorption systems trace a significant fraction of the global [OII] luminosity function. They suggest that star-formation driven outflows are the primary mechanism responsible for $W_r(2796) \gtrsim 1 \text{ \AA}$ absorption systems.

The outflow scenario is further supported by the 500–2000 km s^{-1} winds observed in the high equivalent width and asymmetric MgII absorption profiles seen in spectra of highly star-forming galaxies (Tremonti et al. 2007; Weiner et al. 2009; Martin & Bouché 2009; Rubin et al. 2009). Weiner et al. (2009) further demonstrated that $W_r(2796)$ and outflow velocity correlate with galaxy SFR.

The evidences discussed above for strong MgII systems being produced by star-formation driven winds primarily uses data that have high detection limits such that $W_r(2796) \gtrsim 0.5 \text{ \AA}$ and it is likely that these conclusions apply to systems with $W_r(2796) > 1\text{--}2 \text{ \AA}$. In a sample of 71 absorbing and non-absorbing galaxies consisting of predominantly (85%) $W_r(2796) < 1 \text{ \AA}$ absorption systems, Chen et al. (2010a) do not find a correlation between $W_r(2796)$ and galaxy color and suggest a lack of a physical connection between the MgII halos and recent star formation history of the galaxies. Furthermore, Chen et al. (2010b) found that the MgII halo size scales with the stellar mass and the specific star formation rate of the host galaxy. They interpret this result as massive galaxies having more extended halos and that MgII absorption systems arise from infalling clouds that fuel star formation. Taken together, the Bond et al. (2001b), Bouché et al. (2006), Zibetti et al. (2007), Ménard et al. (2009), and Chen et al. (2010a,b) results may be suggesting that $W_r(2796) < 1\text{--}1.5 \text{ \AA}$ absorption systems are not wind dominated but that larger $W_r(2796)$ systems are wind dominated. Studies that incorporate the gas kinematics, galaxy morphologies and galaxy orientations relative to the quasar line of sight over the full range of $W_r(2796)$ would be useful to examine these ideas.

Kacprzak et al. (2010a) compared MgII absorption and galaxy rotation kinematics of 10, $z \sim 0.5$, $W_r(2796) < 1.4 \text{ \AA}$ systems and found that, in most cases, the absorption was fully to one side of the galaxy systemic velocity and usually aligned with one arm of the rotation curve. These results are consistent with an earlier study of six galaxies by Steidel et al. (2002). However, both studies demonstrated that in virtually all cases, a co-rotating halo model poorly reproduces the MgII absorption velocity spread. This implies that although disk rotation may account for some of the halo gas kinematics, other mechanisms must be invoked to account for the full velocity spreads. In only 3/17 cases studied in this manner, all of which had $W_r(2796) > 1 \text{ \AA}$, the absorption kinematics of the systems displayed possible signatures of winds or superbubbles (Bond et al. 2001a; Ellison et al. 2003; Kacprzak et al. 2010a). Using quasar absorption line methods through cosmological simulations, Kacprzak et al. (2010a) demonstrated that the majority of the MgII absorption arose in an array of structures, such as filaments and tidal streams, which were all infalling toward the galaxy with velocities in the range of the rotation velocity of the simulated galaxy.

Kacprzak et al. (2011) also directly compared the relative MgII halo gas and host galaxy kinematics for 13 $\sim L_*$ galaxies at $z \sim 0.1$. They found that these galaxies had low SFRs, low SFRs per unit area, and their NaID (stellar+ISM tracer) and MgIb (stellar tracer) line ratios implied kinematically quiescent interstellar media containing no strong outflowing gas. Given that these host galaxies were in isolated environments and given the relative halo-gas/galaxy velocity offsets, Kacprzak et al. (2011) suggested a scenario in which the cool halo gas was infalling and providing a gas reservoir that could maintain the low levels of star formation within the host galaxies.

The majority of these studies do not incorporate quantitative morphological and geometric parameters of the host galaxies. Using ground-based imaging studies of MgII absorbing galaxies, Steidel, Dickinson, & Persson (1994) determined that although most galaxy colors are represented, the absorbing galaxies have an average $B - K$ color consistent with that of a local Sb galaxy (also see Zibetti et al. 2007; Chen et al. 2010a). To date, high resolution space-based WFPC-2/*HST* images of MgII absorption-selected galaxies have been used only to qualitatively state that their mor-

phological types appear similar to those of local spiral and elliptical galaxies (Steidel 1998; Chen et al. 2001; Chen & Lanzetta 2003).

In a first effort to quantify morphologies of MgII absorbers, Kacprzak et al. (2007) used a two-dimensional decomposition fitting program GIM2D (Simard et al. 2002) to model the physical structural parameters of galaxies and compared them to MgII absorption properties. They found a correlation between the galaxy morphological asymmetry, normalized by impact parameter, and $W_r(2796)$. Their correlation increases in significance when strong systems [$W_r(2796) > 1.4 \text{ \AA}$] were removed (the greater scatter for stronger systems perhaps suggesting a different mechanism giving rise to the gas in stronger systems). Furthermore, they reported that MgII absorption-selected galaxies have higher levels of morphological perturbations than found for typical field galaxies. Their correlation suggests that known processes responsible for populating halos with gas, such as satellite mergers and longer range galaxy–galaxy interactions, also induce minor perturbations observed in the morphologies of the host galaxies.

The ability to use the WFPC-2/*HST* images for more than measuring magnitudes or impact parameters, by actually quantifying the properties of the galaxies, is a useful way of exploring the absorber–galaxy connection and may shed light on the differences in results found for different equivalent width regimes. In an effort to understand the causal connection between absorbing halo gas and its host galaxy(ies), we expand on our previous work of Kacprzak et al. (2007) and apply GIM2D modeling to WFPC-2/*HST* images to quantify additional morphological properties of known MgII absorbing galaxies. In Kacprzak et al. (2007) we focused on morphological asymmetries of absorption-selected galaxies and how they differ from an “ideal” galaxy, which was modeled by exponential disk and a de Vaucouleurs bulge ($n = 4$). In this paper, we fit a more realistic model to 40 galaxies, 34 from Kacprzak et al. (2007) plus an additional 6 galaxies selected from the literature, using an exponential disk and a Sérsic profile bulge ($0.2 \leq n \leq 4.0$) in order to quantify an additional twelve galaxy morphological parameters. We also compare the galaxy morphological properties to the associated MgII absorption properties (including kinematics) and explore plausible relationships between the absorbing gas and host galaxy properties. In § 2, we describe our sample and analysis. In § 3, we present the measured properties of our sample and identify correlations between galaxy and absorption properties. In § 4, we discuss what can be inferred from the results. Concluding remarks are offered in § 5. Throughout we adopt an $H_0 = 70 \text{ km s}^{-1} \text{ Mpc}^{-1}$, $\Omega_M = 0.3$, $\Omega_\Lambda = 0.7$ cosmology.

2 GALAXY SAMPLE AND DATA ANALYSIS

We have constructed a sample of 40 galaxies, with spectroscopically confirmed redshifts $0.3 < z < 1.0$, selected by the presence of MgII absorption in quasar spectra ($W_r(2796) \geq 0.03 \text{ \AA}$). We selected 34 galaxies from Kacprzak et al. (2007) and 6 additional galaxies found in the literature¹. The absorption properties were measured from HIRES/Keck (Vogt et al. 1994) and UVES/VLT (Dekker et al. 2000) spectra. Galaxy properties were

Table 1. Keck/HIRES and VLT/UVES high resolution quasar observations. The table columns are (1) the quasar field, (2) the quasar redshift, (3) the instrument used, (4) the observation date(s), and (5) the integration time in seconds.

QSO Field	z_{em}	Instrument	Date (UT)	Exposure (seconds)
Q0002+051	1.90	HIRES	1994 Jul. 05	2700
Q0117+213	1.49	HIRES	1995 Jan. 23	5400
Q0229+131	2.06	HIRES	1999 Feb. 08	3600
Q0349–146	0.62	UVES	2005 Oct. 11 ^a	1200
Q0450–132	2.25	HIRES	1995 Jan. 24	5400
Q0454–220	0.53	HIRES	1995 Jan. 22	5400
Q0827+243	0.94	HIRES	1998 Feb. 27	7200
Q0836+113	2.70	HIRES	1998 Feb. 26	5400
Q1038+064	1.27	HIRES	1998 Mar. 01	7200
Q1127–145	1.18	UVES	... ^a	24,900
Q1148+387	1.30	HIRES	1995 Jan. 24	5400
Q1209+107	2.19	UVES	2003 Mar. 12 ^a	14,400
Q1222+228	2.05	HIRES	1995 Jan. 22	3600
Q1241+176	1.27	HIRES	1995 Jan. 22	2400
Q1246–057	2.24	HIRES	1998 Mar. 01	3600
Q1317+277	1.02	HIRES	1995 Jan. 23	3600
Q1354+195	0.72	HIRES	1995 Jan. 22	3600
Q1424–118	0.81	UVES	2005 Jul. 30	1440
Q1622+235	0.93	UVES	2003 Jul. 18 ^a	9800
Q1623+268	2.52	HIRES	1995 Aug. 20 ^b	50,360
Q2128–123	0.50	HIRES	1995 Aug. 20	2500
Q2206–199	2.56	UVES	... ^a	53,503

^a The PID for Q0349–146 is 076.A-0860(A). The Q1127–145 quasar spectrum was obtained over multiple nights. The PIDs for this quasar are 67.A-0567(A) and 69.A-0371(A). The PID for Q1209+107 is 68.A-0170(A). The PID for Q1424–118 is 075.A-0841(A). The PID for Q1622+235 is 69.A-0371(A). The Q2206–199 quasar spectrum was also obtained over multiple nights for PIDs 65.O-0158(A), 072.A-0346(A), and 074.A-0201(A).

^b The Q1623+268 spectrum was obtained over multiple nights; 1995 Aug. 21, 1995 Sept. 10, 1996 May 25, 2005 May 31, 2005 June 01, 2006 Jul. 02, and 2008 Sept. 25.

measured and modeled from F702W or F814W WFPC-2/*HST* images of the quasar fields. Figure 1 summarizes the absorption selection, spectroscopic analysis and morphological fitting technique. Note that three absorbers have two galaxies at the same redshifts (Q0450–132, Q1127–145 and Q1623+268). Since it is possible that a pair of galaxies can give rise to the absorption and such conditions can provide further constraints into the galaxy–absorption connection, we do not exclude these pairs from our sample. Below we describe our data and modeling techniques.

2.1 Quasar Spectroscopy

Details of the HIRES/Keck and UVES/VLT quasar observations are presented in Table 1. The total integrated exposure times for each quasar spectrum ranges from 1200 to 53,303 seconds. The HIRES spectrum of Q0836+113 was reduced using the Mauna Kea Echelle Extraction (MAKEE²) package and the remaining HIRES data were reduced using IRAF³. The UVES data were reduced using the ESO pipeline and the custom code UVES Post–Pipeline

¹ Three galaxies are not used from the Kacprzak et al. (2007) sample: Q1127–145G1 and G2 with $z_{abs} = 0.312710$ were discovered to be in a group of at least five galaxies at similar redshifts close to the quasar line-of-sight (Kacprzak et al. 2010b). Q2206–199G1 with $z_{abs} = 0.751923$ is likely a star (Kacprzak et al. 2010a).

² <http://spider.ipac.caltech.edu/staff/tab/makee>

³ IRAF is written and supported by the IRAF programming group at the National Optical Astronomy Observatories (NOAO) in Tucson, Arizona. NOAO is operated by the Association of Universities for Research in As-

Table 2. *HST*/WFPC-2 Quasar Field Observations. The table columns are (1) the quasar field, (2) the quasar redshift, (2) the quasar right ascension and declination (3), (4) the WFPC-2 filter, (5) the exposure time in seconds, and (6) the proposal identification number and primary investigator of the WFPC-2 observations.

QSO Field	QSO – RA (J2000)	QSO – DEC (J2000)	Filter	Exposure (seconds)	PID/PI
Q0002+051	00:05:20.216	+05:24:10.80	F702W	4600	5984/Steidel
Q0109+200	01:12:10.187	+20:20:21.79	F702W	1800	6303/Disney
Q0117+213	01:20:17.200	+21:33:46.00	F702W	2008	6115/Zuo
Q0150–202	01:52:27.300	–20:01:06.00	F702W	5100	6557/Steidel
Q0229+131	02:31:45.894	+13:22:54.72	F702W	5000	6557/Steidel
Q0235+164	02:38:38.930	+16:36:59.28	F702W	600	5096/Burbidge
Q0349–146	03:51:28.541	–14:29:08.71	F702W	2400	5949/Lanzetta
Q0450–132	04:53:13.556	–13:05:54.91	F702W	2500	5984/Steidel
Q0454–220	04:56:08.900	–21:59:09.00	F702W	1200	5098/Burbidge
Q0827+243	08:30:52.086	+24:10:59.82	F702W	4600	5984/Steidel
Q0836+113	08:39:33.015	+11:12:03.82	F702W	5000	6557/Steidel
Q1019+309	10:22:30.298	+30:41:05.12	F702W	5100	6557/Steidel
Q1038+064	10:41:17.163	+06:10:16.92	F702W	4600	5984/Steidel
Q1127–145	11:30:07.053	–14:49:27.39	F814W	4400	9173/Bechtold
Q1148+387	11:51:29.399	+38:25:52.57	F702W	4800	5984/Steidel
Q1209+107	12:11:40.600	+10:30:02.00	F702W	3600	5351/Bergeron
Q1222+228	12:25:27.389	+22:35:12.72	F702W	5000	5984/Steidel
Q1241+176	12:44:10.826	+17:21:04.52	F702W	5000	6557/Steidel
Q1246–057	12:49:13.800	–05:59:18.00	F702W	4600	5984/Steidel
Q1317+277	13:19:56.316	+27:28:08.60	F702W	4700	5984/Steidel
Q1332+552	13:34:11.700	+55:01:25.00	F702W	2800	6557/Steidel
Q1354+195	13:57:04.437	+19:19:07.37	F702W	2400	5949/Lanzetta
Q1424–118	14:27:38.100	–12:03:50.00	F702W	2100	6619/Lanzetta
Q1511+103	15:13:29.319	+10:11:05.53	F702W	5000	6557/Steidel
Q1622+235	16:24:39.090	+23:45:12.20	F702W	24,000	5304/Steidel
Q1623+268	16:25:48.793	+26:46:58.76	F702W	4600	5984/Steidel
Q2128–123	21:31:35.262	–12:07:04.80	F702W	1800	5143/Mecchitto
Q2206–199	22:08:52.000	–19:43:59.00	F702W	5000	6557/Steidel

Echelle Reduction (UVES POPLER⁴). All the quasar spectra are vacuum and heliocentric velocity corrected.

The quasar spectra are objectively searched for MgII doublet candidates using a detection significance level of 5σ for the $\lambda 2796$ line, and 3σ for the $\lambda 2803$ line. The spectra have detection limits of $W_r(2796) \sim 0.02 \text{ \AA}$ (5σ). Detections and significance levels follow the formalism of Schneider et al. (1993) and Churchill et al. (1999). We define a single MgII system as absorption occurring within $\leq 800 \text{ km s}^{-1}$, but this definition had no effect on our results. A single absorption system may have several kinematic subsystems (see Churchill & Vogt 2001) – absorption regions separated by regions of no detected absorption. Each subsystem is defined in the wavelength regions between where the per pixel equivalent widths become consistent with continuum at the 1σ level.

Analysis of the MgII absorption profiles was performed using our own graphic-based interactive software for local continuum fitting, objective feature identification and measuring absorption properties. We compute the equivalent widths, optical depth weighted mean redshifts (z_{abs}), apparent optical depth column densities (N_a [atoms cm^{-2}]), and flux decrement weighted velocity centroids, widths, and asymmetries ($\langle V \rangle$, W_{vs} , and A [km s^{-1}]), directly from the normalized pixel counts (see Churchill et al. 1999, 2000a; Churchill & Vogt 2001, for the precise definitions of these quanti-

ties). Quantities for the full absorption systems are measured between the pixel of the most blueward extreme and redward extreme subsystems while omitting pixels consistent with continuum (those outside/between the kinematic subsystems).

In many of the MgII systems, corresponding transitions from other elements (such as MgI $\lambda 2853$, FeII $\lambda 2344$, $\lambda 2374$, $\lambda 2383$, $\lambda 2587$, $\lambda 2600$, CaII $\lambda 23935$, $\lambda 3970$, and MnII $\lambda 2577$, $\lambda 2594$, $\lambda 2606$) are detected, which further validates the identification of a MgII system, but are not required to validate a system. In Figure 2 we show an example MgII system that has corresponding transitions from other elements.

In addition to the aforementioned quantities measured directly from the flux decrements, we modeled the absorption profiles using Voigt profile least-square fitting. Voigt profile decomposition provides a means to model each complex absorption profile as multiple individual isothermal “clouds”. Each cloud is parametrized by a velocity center, a column density, and Doppler parameter. The overall decomposition provides a model of the number of clouds (N_{cl}) and their individual Voigt profile parameters.

To best constrain the model, the profile fits simultaneously incorporate all transitions associated with the MgII system. This is particularly useful in cases where the MgII absorption is saturated and there is a loss of component structure. Thus, we use the unsaturated FeII and/or CaII and/or MgI transitions to constrain the number of clouds and velocity centers. All transitions have the same number of clouds and the velocities of the clouds are tied for all transitions. For this work, we assume thermally broadened clouds (no turbulent component), so the b parameters of each cloud are

tronomy (AURA), Inc. under cooperative agreement with the National Science Foundation.

⁴ http://astronomy.swin.edu.au/~mmurphy/UVES_popler.html

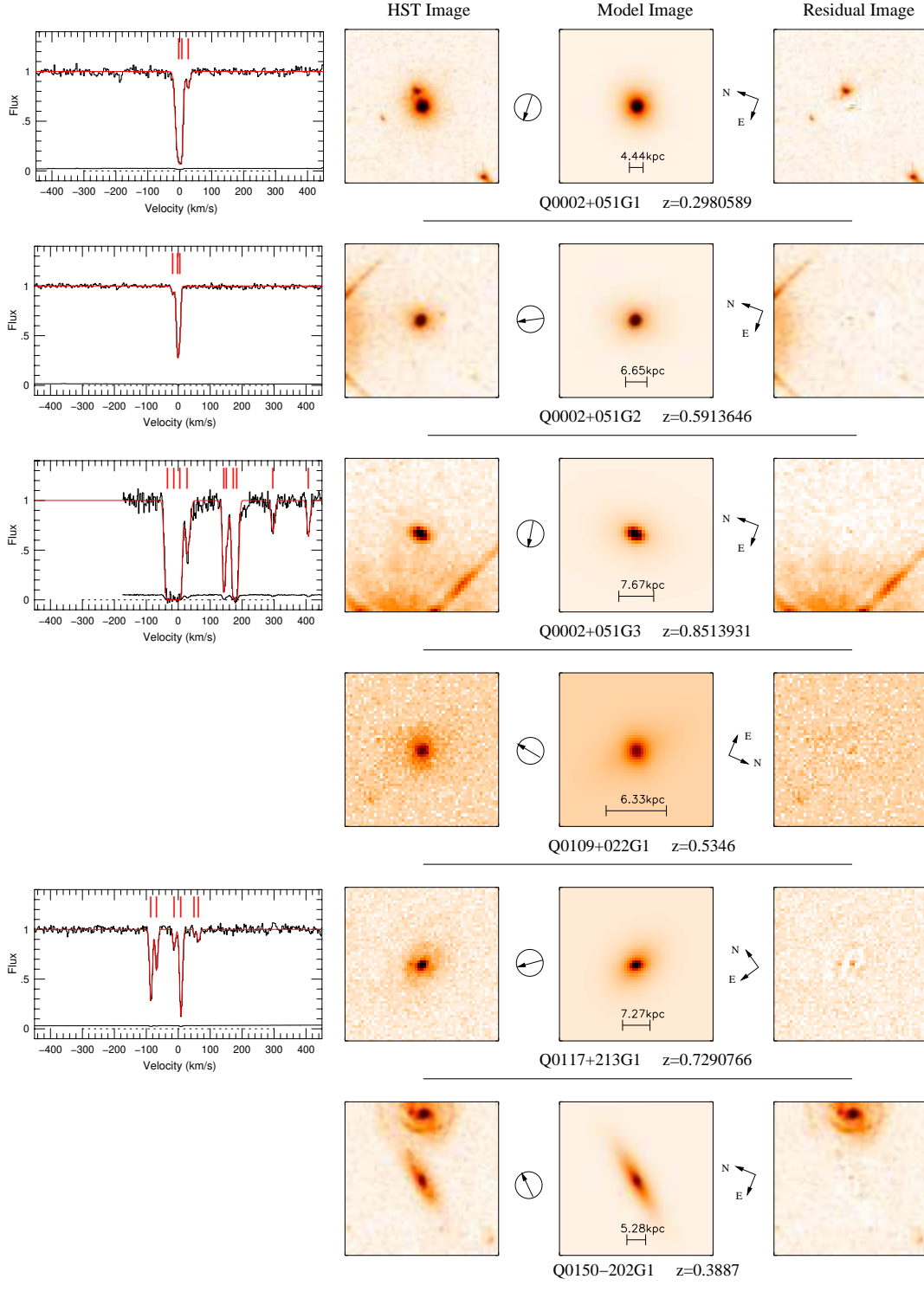


Figure 1. — The full version of this Figure is in the electronic version of the paper, not in the printed version. In the printed version we present a subset of our full sample. — (far-left) The HIRES/Keck or UVES/VLT quasar spectra of the $\text{Mg II } \lambda 2796$ absorption feature are shown alongside the associated absorbing galaxy on the right. The $\text{Mg II } \lambda 2796$ optical depth weight mean absorption redshift is the zeropoint of the velocity scale. The tick marks indicate the number of Voigt profile components and the red curve indicates the fit to the data. We do not have HIRES or UVES data available for six galaxies. (left) WFPC-2/*HST* images of galaxies selected by Mg II absorption. The images are 10 times larger than the 1.5σ isophotal area. — (center) The GIM2D models of the galaxies, which provide quantified morphological parameters. A scale of one arcsecond is indicated on each image along with the physical scale computed at the Mg II absorption redshift. — (right) The residual images from the models, showing quality of the fit and the underlying structure and morphological perturbations of the galaxies. The encircled arrow provides the direction to the quasar (galaxy–quasar orientation). The cardinal directions are also shown and the quasar name and redshift of Mg II absorption is provided under each set of galaxy WFPC-2, model and residual image.

tied for all transitions (yielding the broadening temperature to be the same for all ions). The column densities of transitions belonging to a given ion are tied, but the column densities of different ions are freely fit.

In Figure 2, we show the least-squares Voigt profile model (red) of a saturated MgII doublet with associated transitions from other ions. The number of individual Voigt profile components (N_{cl}), or “clouds”, are indicated with vertical tick marks.

The fitting philosophy is to obtain the minimum number of clouds that provide a statistically reasonable model (i.e., $\chi_\nu \approx 1$). We use the code MINFIT (Churchill 1997), which takes a user input model and performs a least-squares fit while minimizing the number of clouds. With each iteration, the least statistically significant cloud (based upon fractional error criterion) is removed from the model and a new model (less the one cloud) is fit. An F-test is performed to determine whether the two models are statistically consistent at the 97% confidence level. If they are consistent, the cloud is removed from the model. Each cloud not meeting the fractional error criterion is tested in this way until the all clouds meet the criterion and the number of clouds is minimized via the F-test iterations. We applied the fractional error criterion $\sqrt{(dN/N)^2 + (db/b)^2 + (dz/z)^2} < 1.5$, where dN/N , db/b , and dz/z are the column density, b parameter, and redshift fractional errors of the cloud. The resulting models are not sensitive to the input model as long as the input model contains a sufficient number of clouds. For further description of the Voigt profile decomposition of MgII systems see Churchill (1997), Churchill & Vogt (2001), and Churchill, Vogt, & Charlton (2001).

We compute a total system Voigt profile column density, N_{vp} [atoms cm^{-2}], and its uncertainty by summing the individual cloud column densities over the total number of clouds. This number is comparable to the apparent optical depth column density in unsaturated systems, but provides a slightly more robust total column density in saturated systems where the apparent column density provides only a lower limit.

2.2 HST Imaging of Quasar Fields

Details of the WFPC-2/*HST* quasar field observations are presented in Table 2. The WFPC-2/*HST* F702W and F814W images were reduced using the WFPC-2 Associations Science Products Pipeline (WASPP⁵). WASPP data quality verifications include photometric and astrometric accuracy and correctly set zero-points. The F702W filter provides a bandpass similar to a rest-frame Johnson B -band filter for galaxies at $z \sim 0.6$. The F814W filter provides a bandpass similar to the rest-frame B -band for galaxies at $z \sim 0.85$. Galaxy photometry was performed using the Source Extractor (SExtractor) package (Bertin & Arnouts 1996) with a detection criterion of 1.5σ above background with a minimum object area 75 pixels. The m_{F702W} and m_{F814W} magnitudes were measured using the WFPC-2/*HST* zero points (Whitmore 1995), based upon the Vega system.

Galaxy absolute B -band magnitudes, M_B , were determined from the k -corrected observed m_{F702W} or m_{F814W} . To compute the k -corrections, we adopted spectral energy distribution (SED) templates of Kinney et al. (1996). The adopted SED for each galaxy was based upon its rest-frame $B - K$ color obtained from Steidel, Dickinson, & Persson (1994). For galaxies

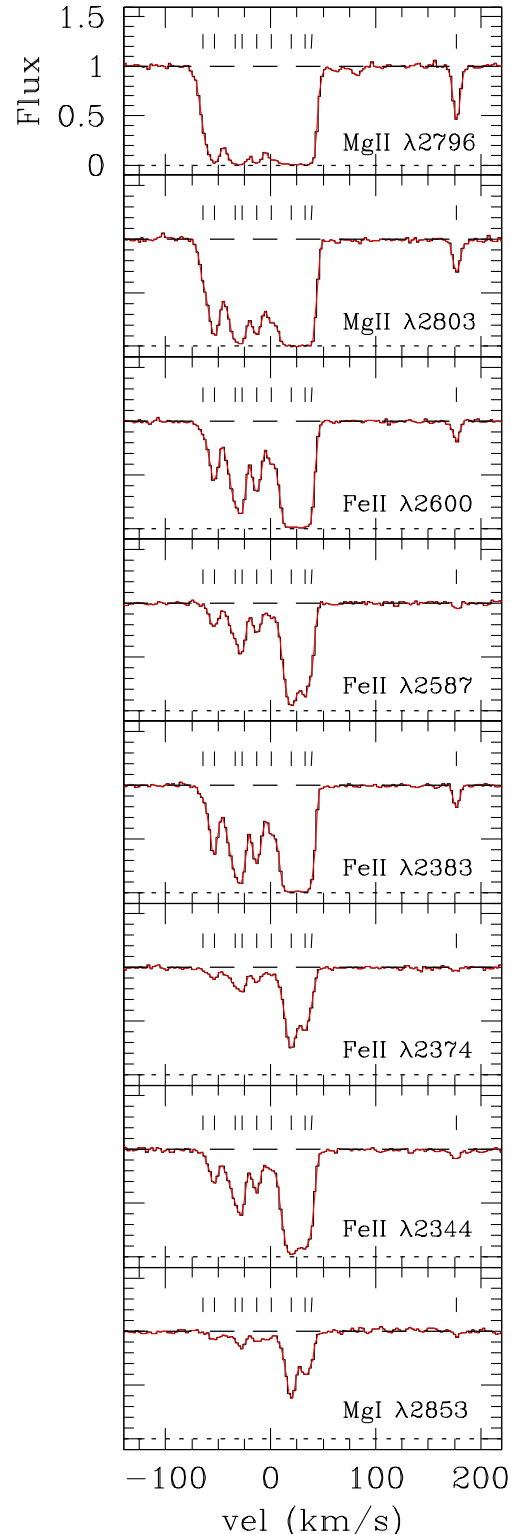


Figure 2. The saturated MgII doublet, FeII and MgI are shown for $z_{abs} = 1.017038$ absorption system seen in the quasar Q2206–199. The Voigt profile fits (red) and the number of individual Voigt profile components (N_{cl}) are indicated with vertical tick marks. The FeII and MgI profiles are used to constrain the kinematics of the saturated MgII profile and to derive MgII column densities.

⁵ Developed by the Canadian Astronomy Data Centre (CADC) and the Space Telescope–European Coordinating Facility (ST–ECF): <http://archive.stsci.edu/hst/wfpc2/pipeline.html>

with no color information, we adopted an Sb SED since this is consistent with the average color of a MgII absorbing galaxy (Steidel, Dickinson, & Persson 1994; Zibetti et al. 2007). B -band luminosities were computed using the DEEP2 optimal M_B^* of Faber et al. (2007, Table 2) in the redshift bin appropriate for each galaxy: M_B^* ranges from -21.07 ($\langle z \rangle = 0.3$) to -21.54 ($\langle z \rangle = 1.1$).

2.3 GIM2D Galaxy Models

For each galaxy, the morphological parameters were quantified by fitting a two-component (bulge+disk) co-spatial parametric model to its two-dimensional surface brightness distribution using GIM2D (Galaxy IMage 2D) (Simard et al. 2002). GIM2D uses the Metropolis algorithm (Metropolis et al. 1953; Saha & Williams 1994), which does not easily fall prey to local minima, to explore the complicated topology of this twelve dimensional parameter space. Once a convergence point is satisfied, the algorithm Monte-Carlo samples the region and keeps acceptable parameter sets, building up a solution probability distribution, which it uses to compute the median of the probability distribution of each free parameter and its 1σ uncertainties. This technique results in an optimal model parameter set and asymmetric errors.

For our 40 galaxies, we fit the surface brightness of the disk component with an exponential profile and we fit the bulge component with a Sérsic profile (Sérsic 1968) where the Sérsic index may vary between $0.2 \leq n \leq 4.0$. These model fits differ from Kacprzak et al. (2007) where we focus was on galaxy asymmetries and how absorption-selected galaxies differ from an ideal galaxy with a de Vaucouleurs bulge and an exponential disk profile. The models have a maximum of twelve free parameters:

- (1.) Galaxy total flux
- (2.) Bulge-to-total fraction (B/T)
- (3.) Bulge semi-major axis effective radius (r_b)
- (4.) Bulge ellipticity ($e_b \equiv 1 - b/a$)
- (5.) Bulge position angle (θ_b)
- (6.) Bulge Sérsic index (n)
- (7.) Disk scale length (r_d)
- (8.) Disk inclination (i)
- (9.) Disk position angle (θ_d)
- (10.) Model center sub-pixel offsets (dx)
- (11.) Model center sub-pixel offsets (dy)
- (12.) Background residual level.

A PSF-deconvolved half-light semi-major axis radius r_h is also computed for each galaxy by integrating the sum of bulge and disk surface brightness profiles out to infinity using the best fitting structural parameters. The half-light radius may be unreliable for cases where there are large differences between the bulge and disk position angles. Additional information regarding the structural parameters derived by GIM2D can be obtained from Simard et al. (2002). GIM2D outputs the various scale length parameters in units of pixels and we use the plate scale of the appropriate WFPC-2 chip to convert to an angular quantity. We then use the plate scale and the angular diameter distance from the adopted cosmology to convert them to linear quantities.

GIM2D uses the isophotal area to extract “portrait size” galaxy images from original images with an area 10 times larger than the 1.5σ galaxy isophotal area, which is chosen such that an accurate background can be computed by GIM2D. During the GIM2D modeling process, the models are convolved with the WFPC-2 point spread function, which was modeled at the appro-

priate locations on the WFPC-2 chip using Tiny Tim (Krist & Hook 2004).

The GIM2D outputs were manually inspected to see if models were realistic representations of the observed galaxies. In addition, we used previously measured galaxy rotation curves to further validate several galaxy models (Kacprzak et al. 2010a; Steidel et al. 2002). In 4/40 cases, we found that the model settled on an unreasonable solution (galaxies Q0454G1, Q1148G1, Q1354G1, and Q2206G2). We reran GIM2D for these four systems using different random seeds, which resulted in more a realistic and stable model. A GIM2D fail-rate of 10% may be less important for large samples of galaxies, however with our smaller sample it is crucial to ensure that we produce representative models.

We note that galaxy asymmetries, and structures such as tidal tails and bars, may affect the galaxy isophotal shape, thereby providing an under/over estimate of the true galaxy shape and orientation. It is difficult to model these disturbed systems and they are not straightforward to interpret. Thus, in cases such as the interacting pair Q0450G1 and Q0450G2, the model inclinations are likely to be biased with respect to the real physical inclination of the disk. Thus, the model results presented here should be interpreted with some caution. However, despite the simplicity of the two-component model (i.e., real galaxies may have more than two smooth components, such as spiral arms, bars, HII regions, etc.), careful analysis of the output models and parameters provides useful information regarding the complexity of galaxies (see Kacprzak et al. 2007).

The impact parameters, D , and their uncertainties are computed using a combination of galaxy isophotal centroids determined by SExtractor and GIM2D model offsets. The dominant uncertainty in D is derived from the pixel offset of the galaxy isophotal center obtained using SExtractor and the isophotal center of the galaxy model determined by GIM2D. This offset is typically about 0.25 pixels. There is also a ~ 0.05 pixel uncertainty in the position of the quasar based upon centroiding errors of unresolved sources in the images.

2.3.1 Galaxy Significance Levels and GIM2D Models

The WFPC-2 image exposure times for our sample range from 600–24,000 seconds, with a typical time of ~ 4700 seconds. It may be of concern that the longest and shortest exposures could yield different measured morphological parameters for similar type galaxies. However, the problem is not so simple since there can be several galaxies of interest in each quasar field image having different apparent magnitudes. Simard et al. (2002) studied sets of GIM2D simulations to characterize the systematic biases and random errors in the galaxy structural measurements. They analyzed simulated WFPC-2 F814W images containing ~ 5500 simulated galaxies. Sky photon noise and detector read-out noise were included along with background noise brightness fluctuations contributed from very faint galaxies below the detection threshold. Simard et al. (2002) determined that the structural parameters can be recovered from the simulated images, equivalent to typical WFPC-2 exposure times of ~ 2800 – 4400 s, and that the uncertainties only become significant when $m_{F814W} > 23.5$. Only two of our galaxies have apparent magnitudes above the Simard limit with the remaining below $m_{HST} = 22.6$. Both of those galaxies have $m_{HST} = 23.6$ and are in a WFPC-2 image that has a typical exposure time of 5000 seconds.

Here we examine the significance level (SL) for each galaxy in our sample, which is defined by the ratio of the galaxy measured flux and the flux uncertainty (see Table 3). The SL is then

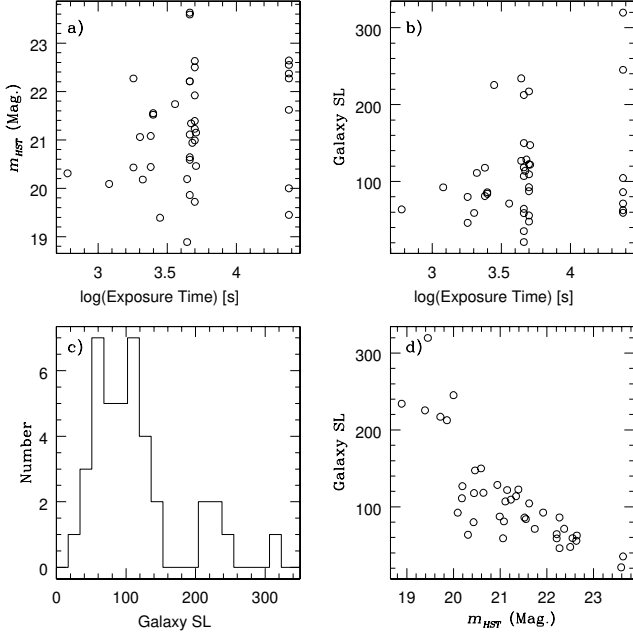


Figure 3. — (a) The apparent magnitude as a function of exposure time for the 40 MgII absorption-selected galaxies in our sample. — (b) Galaxy significance level (SL) as a function of exposure time. — (c) Galaxy SL distribution. — (d) Galaxy SL as a function of galaxy apparent magnitude. Note that the galaxy SL is only dependent m_{HST} and not the WFPC-2 exposure time.

equivalent to an average signal-to-noise ratio per pixel, with higher weighting towards the bright pixels. In Figure 3a, we show the distribution of galaxy apparent magnitudes as a function of exposure time. All exposure times cover a wide range of apparent magnitudes. We see no trends with exposure time.

In Figure 3b, we show the distribution of SL as a function of exposure time. There is a wide range of SL for each exposure time. In Figure 3c, we show the binned distribution of SL . The majority of galaxies lie within the main peak around $SL \sim 80$ with others, not necessarily from long exposures, at higher SL . In Figure 3d, we show the SL as a function of galaxy apparent magnitude. Note the strong anti-correlation. The anti-correlation exhibits some dispersion which can be attributed to background Poisson noise and also some variance in the galaxy surface brightness for a given magnitude.

The strong anti-correlation between SL and m_{HST} suggests that the galaxy SL primarily depends on its apparent magnitude and not on the exposure time. Therefore, degrading individual quasar field images to a lower signal-to-noise ratio is not necessary for the galaxy magnitude range of interest ($m_{HST} < 23.5$). We discuss additional tests regarding S/N and quasar PSF near absorbing galaxies in Kacprzak et al. (2007).

3 RESULTS

3.1 The Sample

We have constructed a sample of 40 MgII absorption-selected galaxies between $0.3 < z < 1.0$. In Figure 1 we show WFPC-2 portraits of the galaxies. Note that the galaxy images are 10 times larger than the 1.5σ galaxy isophotal area, giving the galaxies the

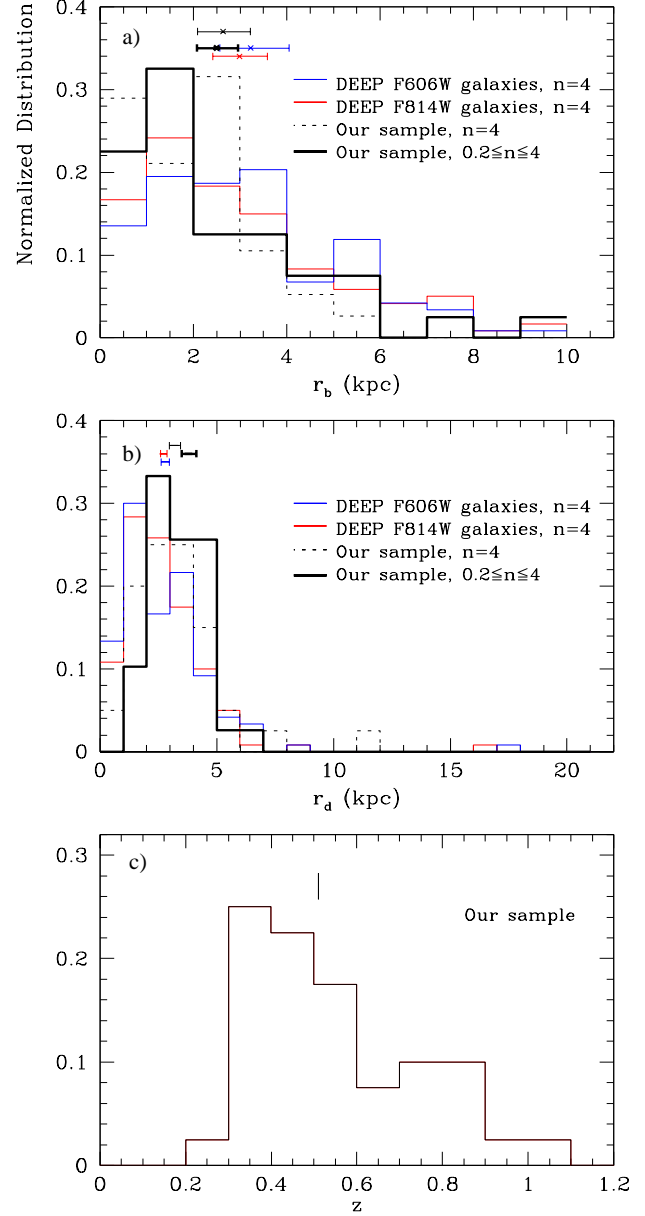


Figure 4. — (a) The normalized distributions of the bulge effective radii derived for 120 galaxies from DEEP survey imaged with the F606W filter using a fixed Sérsic index of $n = 4$ (blue), 120 galaxies from DEEP survey imaged with the F814W filter also using $n = 4$ (red), our sample having free Sérsic index fits (solid black), and our sample fit with $n = 4$ (dotted black). The mean values are also shown and the error bars represent the average uncertainty from the model fits of all galaxies. All samples have similar bulge effective radii distributions. — (b) same as (a) except plotted for the disk scale length distributions. Samples have similar distributions except our sample has larger disk scale lengths. Note that when the Sérsic index is fixed at $n = 4$, the disk scale length distribution shifts towards smaller sizes and becomes more consistent with the DEEP sample. — (c) the redshift distributions for the 40 galaxies from our sample. The mean redshift value is indicated. The 120 DEEP galaxies have been selected to have the same redshift distribution as our sample.

Table 3. The observed galaxy properties. The columns are (1) the quasar name and galaxy ID number, (2) the optical depth weighted mean Mg II $\lambda 2796$ absorption redshift, (3) the Mg II $\lambda 2796$ rest-frame equivalent width, (4) the source of the adopted equivalent width measurements, (5) the adopted galaxy redshift, (6) the source(s) of galaxy spectroscopic redshift, (7) the projected galaxy–quasar separation (impact parameter), (8) the WFPC-2/HST F702W or F814W galaxy apparent magnitude, (9) galaxy significance level in the WFPC-2 images, defined to be the ratio of the measured galaxy flux and the flux uncertainty, (10) the $B - K$ colors, (11) the rest-frame B -band galaxy absolute magnitude, and (12) the galaxy B -band luminosity.

QSO field & Galaxy ID	z_{abs}	$W_r(2796)$ (Å)	Ref ^a	z_{gal}	Ref ^b	D (kpc)	m_{HST}	SL	$B-K$	M_B	L_B (L^*)
Q0002+051G1	0.298059	0.244 ± 0.003	1	0.298	1	59.7 ± 0.3	19.86 ± 0.01	212.6	4.02	-19.64	0.27
Q0002+051G2	0.591365	0.102 ± 0.002	1	0.592	1	36.3 ± 0.3	21.11 ± 0.01	106.9	4.12	-20.78	0.71
Q0002+051G3	0.851393	1.089 ± 0.008	1	0.85180	2	26.0 ± 0.4	22.21 ± 0.02	64.4	2.86	-21.27	0.92
Q0109+200G1	0.5346	2.26	2	0.534	3,4	45.1 ± 0.1	22.27 ± 0.02	46.1	3.90	-19.20	0.17
Q0117+213G1	0.729077	0.244 ± 0.005	1	0.729	1	55.8 ± 0.3	21.06 ± 0.02	59.0	4.02	-21.81	1.32
Q0150-202G1	0.3887	0.58 ± 0.05	2	0.383	3,4	60.6 ± 0.7	21.15 ± 0.01	121.8	...	-19.26	0.19
Q0229+131G1	0.417338	0.816 ± 0.020	1	0.4167	2,3,4	37.1 ± 0.5	19.72 ± 0.01	217.1	3.92	-20.83	0.74
Q0235+164G1	0.524	2.34 ± 0.05	3	0.524	4	12.2 ± 0.2	20.31 ± 0.02	63.6	...	-21.10	0.95
Q0349-146G1	0.357168	0.175 ± 0.007	1	0.3567	5	71.9 ± 0.3	20.44 ± 0.01	117.8	...	-19.70	0.28
Q0450-132G1	0.493936	0.674 ± 0.024	1	0.4941	1,2	50.1 ± 0.1	21.55 ± 0.01	84.0	3.41	-19.65	0.25
Q0450-132G2	0.493936	0.674 ± 0.024	1	0.4931	1,2	62.8 ± 0.1	21.52 ± 0.01	86.0	3.41	-19.69	0.26
Q0454-220G1	0.483337	0.426 ± 0.007	1	0.48382	2,5	107.8 ± 0.8	20.09 ± 0.01	92.3	...	-21.03	0.90
Q0827+243G1	0.524966	2.419 ± 0.012	1	0.5247	6	37.5 ± 0.3	20.64 ± 0.01	118.2	4.01	-20.75	0.69
Q0836+113G1	0.786725	2.133 ± 0.019	1	0.78682	2,7	26.9 ± 0.5	22.63 ± 0.02	55.8	3.00	-20.48	0.39
Q1019+309G1	0.3461	0.70 ± 0.07	4	0.346	1	46.3 ± 0.1	20.46 ± 0.01	147.3	3.10	-19.59	0.26
Q1038+064G1	0.441453	0.673 ± 0.011	1	0.4432	8	56.2 ± 0.3	20.59 ± 0.01	149.9	4.43	-20.15	0.40
Q1127-145G1	0.328279	0.028 ± 0.003	1	0.32839	9	76.9 ± 0.4	20.19 ± 0.01	126.8	...	-19.16	0.17
Q1127-145G2	0.328279	0.028 ± 0.003	1	0.32847	2	91.4 ± 0.2	18.89 ± 0.00	234.1	...	-20.46	0.57
Q1148+387G1	0.553363	0.640 ± 0.013	1	0.5536	8	20.6 ± 0.3	20.94 ± 0.01	128.4	3.59	-20.68	0.65
Q1209+107G1	0.392924	1.187 ± 0.005	1	0.392	3	37.9 ± 0.1	21.74 ± 0.02	71.2	1.89	-18.60	0.10
Q1222+228G1	0.550198	0.094 ± 0.009	1	0.5502	8	38.0 ± 0.6	22.50 ± 0.02	47.7	3.80	-19.08	0.15
Q1241+176G1	0.550482	0.465 ± 0.011	1	0.550	1	21.2 ± 0.3	21.39 ± 0.01	122.5	3.42	-20.21	0.42
Q1246-057G1	0.639909	0.450 ± 0.004	1	0.637	1	29.3 ± 0.9	22.21 ± 0.02	58.8	3.78	-20.02	0.25
Q1317+277G1	0.660049	0.320 ± 0.006	1	0.6610	8	103.9 ± 0.5	21.34 ± 0.01	113.8	...	-20.97	0.61
Q1332+552G1	0.374	2.90	2	0.373	10	28.0 ± 0.3	19.39 ± 0.00	225.5	3.95	-20.79	0.77
Q1354+195G1	0.456598	0.773 ± 0.015	1	0.4592	11	45.3 ± 0.5	21.08 ± 0.01	81.0	3.04	-19.85	0.30
Q1424-118G1	0.341716	0.100 ± 0.015	1	0.3404	12	86.8 ± 0.4	20.18 ± 0.01	111.1	...	-19.83	0.32
Q1511+103G1	0.4369	0.454 ± 0.046	5	0.437	3,4	38.3 ± 0.4	21.23 ± 0.01	109.3	3.02	-19.56	0.23
Q1622+235G1	0.317597	0.491 ± 0.010	1	0.3181	13	54.8 ± 0.2	20.00 ± 0.00	245.2	4.09	-19.68	0.28
Q1622+235G2	0.368112	0.247 ± 0.005	1	0.3675	13	114.5 ± 0.1	19.45 ± 0.00	319.7	...	-20.79	0.77
Q1622+235G3	0.471930	0.769 ± 0.006	1	0.4720	13	34.3 ± 0.2	22.27 ± 0.01	86.1	2.71	-18.76	0.11
Q1622+235G4	0.656106	1.446 ± 0.006	1	0.6560	13	100.0 ± 0.7	22.55 ± 0.02	59.2	2.49	-19.71	0.19
Q1622+235G5	0.702902	0.032 ± 0.003	1	0.7016	13	113.2 ± 0.5	21.62 ± 0.01	104.4	...	-20.97	0.61
Q1622+235G6	0.797078	0.468 ± 0.008	1	0.7975	13	71.8 ± 0.7	22.37 ± 0.02	71.3	3.04	-20.80	0.52
Q1622+235G7	0.891276	1.548 ± 0.004	1	0.8909	13	23.4 ± 0.2	22.64 ± 0.02	62.6	3.10	-21.04	0.74
Q1623+268G1	0.887679	0.903 ± 0.004	1	0.888	1	48.2 ± 0.5	23.63 ± 0.03	35.4	3.97	-20.29	0.37
Q1623+268G2	0.887679	0.903 ± 0.004	1	0.888	1	72.0 ± 0.2	23.59 ± 0.05	21.2	...	-20.07	0.30
Q2128-123G1	0.429735	0.395 ± 0.010	1	0.430	3,4	48.4 ± 0.2	20.43 ± 0.01	79.9	3.26	-20.32	0.46
Q2206-199G1	0.948361	0.249 ± 0.002	1	0.948	3	87.6 ± 0.7	21.92 ± 0.01	92.5	...	-22.02	1.83
Q2206-199G2	1.017038	1.047 ± 0.003	1	1.01655	3,2	105.2 ± 0.6	20.99 ± 0.01	87.4	...	-23.79	7.96

^aMg II Absorption Measurements: (1) This paper (2) Guillemin & Bergeron (1997), (3) Lanzetta & Bowen (1992), (4) Steidel & Sargent (1992), and (5) Foltz et al. (1986).

^bGalaxy Identification: (1) Steidel, Dickinson, & Persson (1994), (2) Kacprzak et al. (2010a), (3) Bergeron & Boissé (1991), (4) Guillemin & Bergeron (1997), (5) Chen et al. (1998), (6) Kanekar & Chengalur (2001a), (7) Lowenthal et al. (1990), (8) Steidel et al. (2002), (9) Kacprzak et al. (2010b), (10) Miller, Goodrich, & Stephens (1987), (11) Ellingson et al. (1991), (12) Chen et al. (2001), and (13) Steidel et al. (1997).

appearance of all being of similar size; the angular and physical scales of each galaxy image is shown. The encircled arrow next to the portrait provides the direction to the quasar relative to the galaxy. In Table 3 we list the observed galaxy properties for the sample, which were mostly derived from the WFPC-2 images. The galaxies range between $-18.6 \leq M_B \leq -23.8$ and have a impact parameter range of $12 \leq D \leq 115$ kpc.

Also in Figure 1 we show the fitted Mg II $\lambda 2796$ absorption profiles. The number of clouds is indicated by the tickmarks above the fit. We do not have in hand the high resolution spectra of six

Mg II systems so we can only use their equivalent widths in our analysis. Note the wide variety of Mg II $\lambda 2796$ profile velocity widths and structures. The Mg II rest-frame equivalent widths range between $0.03 \leq W_r(2796) \leq 2.9$ Å. In Table 4 we present the Mg II absorption properties measured from the profiles and obtained from the Voigt profiles fits.

Along with the *HST* images shown in Figure 1, we also include the galaxy GIM2D model and residual images. The model and residual image is displayed using the same dynamic range as the WFPC-2 image. As mentioned above, the smooth GIM2D mod-

Table 4. Summary of the Mg II $\lambda 2796$ absorption properties. The table columns are (1) the quasar name and galaxy ID number, (2) the optical depth weighted mean Mg II $\lambda 2796$ absorption redshift, (3) the rest-frame equivalent width $W_r(2796)$, (4) the doublet ratio (DR), (5) the number of clouds (N_{cl}), (6) the Voigt profiles fitted system column density (N_{vp}), (7) the Mg II optical depth, (8) The AOD derived column density (N_a), (9) the mean velocity ($\langle V \rangle$), (10) the velocity spread, (W_{vs}), and (9) the velocity asymmetry (A).

QSO field & Galaxy ID	z_{abs}	$W_r(2796)$ (Å)	DR	N_{cl}	$\log(N_{vp})$ (cm ⁻²)	τ^a	$\log(N_a)^a$ (cm ⁻²)	$\langle V \rangle$ (km s ⁻¹)	W_{vs} (km s ⁻¹)	A (km s ⁻¹)
Q0002+051G1	0.298058	0.244±0.003	1.34±0.03	3	13.14±0.02	54.1 ^{+8.6} _{-9.9}	13.08 ^{+0.07} _{-0.08}	0.12±0.33	11.6±0.4	0.33±0.06
Q0002+051G2	0.591363	0.102±0.002	1.54±0.04	3	12.61±0.04	16.0 ^{+3.0} _{-3.2}	12.55 ^{+0.08} _{-0.09}	-0.39±0.29	7.0±0.5	-0.41±0.25
Q0002+051G3	0.851349	1.089±0.008	1.16±0.01	10	14.43±0.04	406.8 ^{+22.1} _{-22.8}	13.95 ^{+0.02} _{-0.02}	78.36±1.20	112.5±1.5	0.95±0.02
Q0109+200G1	0.5346	2.26
Q0117+213G1	0.729104	0.244±0.005	1.84±0.09	6	13.05±0.02	38.5 ^{+4.3} _{-5.1}	12.93 ^{+0.05} _{-0.06}	-29.54±1.28	48.5±1.0	0.86±0.21
Q0150-202G1	0.388700	0.580±0.050
Q0229+131G1	0.417316	0.816±0.020	1.16±0.04	6	13.84±0.03	186.4 ^{+9.5} _{-19.8}	13.61 ^{+0.02} _{-0.05}	8.56±2.91	64.7±5.6	1.08±0.08
Q0235+164G1	0.524	2.34±0.05
Q0349-146G1	0.357161	0.175±0.007	1.17±0.07	3	13.87±0.17	38.0 ^{+6.2} _{-8.9}	12.92 ^{+0.07} _{-0.10}	-24.47±2.20	43.5±2.1	-2.48±0.13
Q0450-132G1	0.493929	0.674±0.024	1.19±0.06	6	14.74±2.77	>114.6	>13.70	-1.86±1.19	24.3±1.2	-0.20±0.07
Q0450-132G2	0.493929	0.674±0.024	1.19±0.06	6	14.74±2.77	>114.6	>13.70	-1.86±1.19	24.3±1.2	-0.20±0.07
Q0454-220G1	0.483319	0.426±0.007	1.33±0.04	6	13.69±0.10	>70.6	>13.49	-4.19±0.59	19.6±0.7	-0.34±0.04
Q0827+243G1	0.524988	2.419±0.012	1.04±0.01	13	15.25±0.05	>640.5	>14.45	4.20±0.50	78.7±0.4	0.09±0.02
Q0836+113G1	0.786731	2.113±0.019	1.05±0.01	20	15.54±2.29	>527.2	>14.37	0.95±0.70	67.5±0.5	0.13±0.01
Q1019+309G1	0.3461	0.70±0.07
Q1038+064G1	0.441503	0.673±0.011	1.34±0.04	7	13.73±0.04	92.8 ^{+12.2} _{-8.3}	13.61 ^{+0.04} _{-0.04}	10.39±0.88	40.3±0.7	0.36±0.03
Q1127-145G1	0.328112	0.028±0.003	1.56±0.25	2	11.92±0.03	3.4 ^{+0.5} _{-0.7}	11.87 ^{+0.07} _{-0.09}	49.34±5.49	61.3±2.9	13.19±1.76
Q1127-145G2	0.328112	0.028±0.003	1.56±0.25	2	11.92±0.03	3.4 ^{+0.5} _{-0.7}	11.87 ^{+0.07} _{-0.09}	49.34±5.49	61.3±2.9	13.19±1.66
Q1148+387G1	0.553499	0.640±0.013	1.75±0.07	8	13.48±0.02	113.4 ^{+8.3} _{-12.8}	13.40 ^{+0.03} _{-0.05}	-2.69±1.24	49.2±1.0	0.24±0.17
Q1209+107G1	0.392857	1.187±0.005	1.44±0.01	12	13.94±0.06	258.5 ^{+17.9} _{-20.8}	13.76 ^{+0.03} _{-0.04}	-40.39±0.49	95.9±0.4	-0.66±0.01
Q1222+228G1	0.550188	0.094±0.009	1.56±0.24	3	12.45±0.12	11.0 ^{+1.1} _{-2.1}	12.38 ^{+0.04} _{-0.08}	-0.63±1.61	13.0±1.5	-0.98±0.34
Q1241+176G1	0.550493	0.465±0.011	1.29±0.04	4	13.64±0.07	95.8 ^{+5.6} _{-8.2}	13.32 ^{+0.03} _{-0.04}	10.18±1.53	41.5±2.3	1.07±0.06
Q1246-057G1	0.639913	0.450±0.004	1.18±0.02	3	13.75±0.10	>101.3	>13.65	0.85±0.30	15.9±0.4	0.14±0.06
Q1317+277G1	0.660051	0.320±0.006	1.61±0.06	6	13.14±0.07	53.5 ^{+5.8} _{-6.9}	13.07 ^{+0.05} _{-0.06}	22.46±0.98	41.4±0.9	1.18±0.04
Q1332+552G1	0.374	2.90
Q1354+195G1	0.456605	0.773±0.015	1.33±0.04	6	13.91±0.38	174.4 ^{+10.2} _{-20.0}	13.58 ^{+0.03} _{-0.05}	-8.65±0.94	35.1±0.9	-0.35±0.02
Q1424-118G1	0.341712	0.100±0.015	1.87±0.39	1	12.61±0.06	20.2 ^{+2.0} _{-7.3}	12.65 ^{+0.04} _{-0.16}	0.09±1.033	3.7±1.3	-0.26±0.37
Q1511+103G1	0.4369	0.454±0.046
Q1622+235G1	0.317712	0.491±0.010	1.23±0.04	6	13.88±0.58	112.0 ^{+6.6} _{-8.9}	13.39 ^{+0.03} _{-0.04}	26.06±0.98	41.4±0.8	0.64±0.02
Q1622+235G2	0.368106	0.247±0.005	1.25±0.05	3	13.21±1.13	45.7 ^{+5.4} _{-6.7}	13.00 ^{+0.05} _{-0.06}	-2.03±0.42	11.4±0.4	-0.27±0.06
Q1622+235G3	0.471928	0.769±0.006	1.19±0.02	8	14.04±0.20	147.4 ^{+14.4} _{-11.2}	13.81 ^{+0.04} _{-0.03}	-0.32±0.38	28.1±0.4	-0.16±0.03
Q1622+235G4	0.656069	1.446±0.006	1.10±0.01	17	15.18±0.06	545.6 ^{+12.4} _{-17.5}	14.08 ^{+0.01} _{-0.01}	-6.42±0.34	46.0±0.3	-0.13±0.02
Q1622+235G5	0.702904	0.032±0.003	1.61±0.27	1	12.09±0.05	4.4 ^{+0.9} _{-1.2}	11.98 ^{+0.09} _{-0.12}	0.41±0.63	2.4±1.1	0.80±0.67
Q1622+235G6	0.797061	0.468±0.008	1.62±0.05	6	13.28±0.01	79.7 ^{+7.1} _{-8.3}	13.24 ^{+0.04} _{-0.04}	-9.92±1.24	55.5±1.4	-0.96±0.06
Q1622+235G7	0.891190	1.548±0.004	1.09±0.01	10	15.07±0.02	>529.3	>14.37	-13.42±0.22	52.2±0.2	-0.18±0.01
Q1623+268G1	0.887679	0.903±0.004	1.25±0.01	10	14.58±0.03	219.0 ^{+20.8} _{-17.4}	13.68 ^{+0.04} _{-0.04}	5.42±0.35	75.0±0.25	0.45±0.01
Q1623+268G2	0.887679	0.903±0.004	1.25±0.01	10	14.58±0.03	219.0 ^{+20.8} _{-17.4}	13.68 ^{+0.04} _{-0.04}	5.42±0.35	75.0±0.25	0.45±0.01
Q2128-123G1	0.429708	0.395±0.010	1.17±0.05	5	14.06±0.36	94.4 ^{+13.4} _{-14.6}	13.32 ^{+0.06} _{-0.07}	-5.45±0.91	19.3±1.0	-0.38±0.05
Q2206-199G1	0.948381	0.249±0.002	1.33±0.02	5	13.25±0.07	55.2 ^{+8.1} _{-8.5}	13.09 ^{+0.06} _{-0.07}	-23.84±0.35	41.3±0.2	-1.45±0.01
Q2206-199G2	1.016979	1.047±0.003	1.14±0.01	10	14.67±0.04	405.2 ^{+26.5} _{-32.5}	13.95 ^{+0.03} _{-0.04}	-2.13±0.34	49.0±0.6	0.53±0.01

^a In cases where the Mg II $\lambda 2796$ absorption is saturated, we use the Mg II $\lambda 2803$ absorption profile to compute $\log(N_a)$ and τ . The Mg II $\lambda 2796$ and Mg II $\lambda 2803$ absorption profiles are both saturated in only six cases.

Table 5. The Mg II absorbing galaxy morphological properties, which were obtained from GIM2D modeling of the WFPC-2/*HST* images. The table columns are (1) the quasar name and galaxy ID number, (2) the optical depth weighted mean Mg II $\lambda 2796$ absorption redshift (z_{abs}), (3) the Mg II $\lambda 2796$ rest-frame equivalent width $W_r(2796)$, (4) the bulge-to-total fraction (B/T), (5) the bulge Sérsic index (n) (6) the bulge semi-major axis effective radius (r_b), (7) the bulge ellipticity ($e_b \equiv 1 - b/a$), (8) the bulge position angle (θ_b), (9) the semi-major axis disk scale length (r_d), (10) the disk inclination (i), (11) the disk position angle (θ_d), (12) the galaxy half light radius (r_h), and (13) the χ^2 per degree of freedom for the fit.

QSO Field	z_{abs}	$W_r(2796)$ (Å)	B/T	n	r_b (kpc)	e_b	θ_b (deg)	r_d (kpc)	i (deg)	θ_d (deg)	r_h (kpc)	χ^2
Q0002+051G1	0.298059	0.244±0.003	0.41 ^{+0.06} _{-0.07}	2.9 ^{+0.5} _{-0.4}	1.3 ^{+0.3} _{-0.3}	0.13 ^{+0.05} _{-0.03}	65 ⁺¹¹ ₋₁₃	3.2 ^{+0.1} _{-0.1}	29.5 ^{+2.4} _{-4.5}	50 ⁺¹² ₋₈	3.47	0.97
Q0002+051G2	0.591365	0.102±0.002	0.41 ^{+0.06} _{-0.05}	1.8 ^{+0.6} _{-0.7}	0.9 ^{+0.2} _{-0.1}	0.19 ^{+0.09} _{-0.09}	18 ⁺¹² ₋₁₃	4.1 ^{+0.6} _{-0.6}	40.7 ^{+4.3} _{-3.7}	77 ⁺¹⁰ ₋₁₀	3.35	0.97
Q0002+051G3	0.851393	1.089±0.008	0.45 ^{+0.06} _{-0.04}	0.5 ^{+0.5} _{-0.3}	1.1 ^{+0.1} _{-0.1}	0.55 ^{+0.09} _{-0.09}	20 ⁺⁴ ₋₅	4.0 ^{+0.5} _{-0.5}	48.1 ^{+6.7} _{-10.5}	7 ⁺¹² ₋₁₂	2.47	0.87
Q0109+200G1	0.5346	2.26	0.52 ^{+0.14} _{-0.12}	1.4 ^{+0.5} _{-0.4}	1.3 ^{+0.2} _{-0.2}	0.26 ^{+0.26} _{-0.12}	34 ⁺¹⁴ ₋₁₇	2.5 ^{+0.4} _{-0.6}	65.2 ^{+6.4} _{-7.0}	47 ⁺¹³ ₋₈	2.24	0.92
Q0117+213G1	0.729077	0.244±0.005	0.24 ^{+0.17} _{-0.09}	3.7 ^{+0.3} _{-1.4}	1.0 ^{+1.1} _{-0.7}	0.46 ^{+0.14} _{-0.10}	90 ⁺¹³ ₋₂₃	3.3 ^{+0.9} _{-0.5}	45.4 ^{+12.1} _{-7.0}	51 ⁺¹¹ ₋₁₀	4.41	0.97
Q0150-202G1	0.3887	0.580±0.050	0.13 ^{+0.02} _{-0.03}	3.5 ^{+0.2} _{-0.2}	2.1 ^{+0.4} _{-0.5}	0.39 ^{+0.08} _{-0.08}	88 ⁺¹⁶ ₋₁₃	4.6 ^{+0.2} _{-0.2}	76.4 ^{+0.7} _{-1.0}	81 ⁺¹ ₋₁	7.03	0.99
Q0229+131G1	0.417338	0.816±0.020	0.29 ^{+0.01} _{-0.01}	1.2 ^{+0.1} _{-0.1}	1.2 ^{+0.0} _{-0.0}	0.17 ^{+0.03} _{-0.03}	38 ⁺⁶ ₋₆	6.7 ^{+0.2} _{-0.2}	51.4 ^{+1.0} _{-1.3}	82 ⁺¹ ₋₁	7.36	1.37
Q0235+164G1	0.524	2.34±0.05	0.33 ^{+0.03} _{-0.02}	1.9 ^{+2.1} _{-1.7}	0.1 ^{+0.1} _{-0.1}	0.59 ^{+0.11} _{-0.19}	54 ⁺⁶³ ₋₁₀₂	3.2 ^{+0.4} _{-0.4}	42.0 ^{+5.4} _{-7.9}	10 ⁺¹⁴ ₋₁₃	3.10	1.19
Q0349-146G1	0.357168	0.175 ± 0.007	0.27 ^{+0.08} _{-0.04}	0.3 ^{+0.1} _{-0.1}	3.1 ^{+0.1} _{-0.2}	0.46 ^{+0.06} _{-0.05}	62 ⁺⁴ ₋₃	2.3 ^{+0.2} _{-0.1}	56.3 ^{+5.6} _{-4.0}	77 ⁺⁸ ₋₇	3.66	1.16
Q0450-132G1	0.493936	0.674 ± 0.024	0.55 ^{+0.05} _{-0.05}	0.8 ^{+0.1} _{-0.1}	1.7 ^{+0.1} _{-0.1}	0.55 ^{+0.03} _{-0.03}	22 ⁺³ ₋₂	3.5 ^{+0.2} _{-0.4}	60.0 ^{+0.0} _{-1.1}	62 ⁺³ ₋₃	2.68	3.45
Q0450-132G2	0.493936	0.674±0.024	0.62 ^{+0.06} _{-0.03}	0.7 ^{+0.2} _{-0.1}	1.8 ^{+0.1} _{-0.1}	0.70 ^{+0.00} _{-0.01}	11 ⁺² ₋₂	2.6 ^{+0.1} _{-0.2}	63.6 ^{+3.0} _{-3.6}	23 ⁺⁶ ₋₄	2.32	1.63
Q0454-220G1	0.483337	0.426 ± 0.007	0.00 ^{+0.10} _{-0.00}	3.9 ^{+0.1} _{-0.1}	4.2 ^{+0.4} _{-0.1}	0.37 ^{+0.01} _{-0.01}	2 ⁺¹ ₋₇	4.9 ^{+0.1} _{-0.2}	42.1 ^{+2.7} _{-3.1}	5 ⁺⁴ ₋₄	8.26	1.16
Q0827+243G1	0.524966	2.419±0.012	0.00 ^{+0.01} _{-0.00}	4.0 ^{+0.0} _{-0.1}	2.9 ^{+1.1} _{-0.5}	0.32 ^{+0.02} _{-0.02}	77 ⁺⁸ ₋₃	4.6 ^{+0.1} _{-0.1}	74.4 ^{+0.6} _{-0.7}	87 ⁺¹ ₋₁	7.64	1.38
Q0836+113G1	0.786725	2.133±0.019	0.48 ^{+0.09} _{-0.08}	0.3 ^{+0.2} _{-0.1}	4.0 ^{+0.4} _{-0.3}	0.70 ^{+0.00} _{-0.04}	17 ⁺⁴ ₋₃	2.3 ^{+0.2} _{-0.1}	84.9 ^{+0.1} _{-1.1}	32 ⁺² ₋₁	4.36	1.31
Q1019+309G1	0.3461	0.70±0.07	0.33 ^{+0.04} _{-0.04}	0.2 ^{+0.1} _{-0.0}	2.3 ^{+0.1} _{-0.1}	0.51 ^{+0.03} _{-0.02}	6 ⁺² ₋₂	1.9 ^{+0.1} _{-0.1}	38.6 ^{+4.5} _{-3.4}	10 ⁺⁷ ₋₇	2.91	1.07
Q1038+064G1	0.441453	0.673±0.011	0.73 ^{+0.08} _{-0.09}	0.6 ^{+0.1} _{-0.1}	4.6 ^{+0.1} _{-0.1}	0.64 ^{+0.01} _{-0.02}	86 ⁺¹ ₋₁	4.1 ^{+0.3} _{-0.3}	49.8 ^{+7.4} _{-5.2}	78 ⁺⁴ ₋₄	5.04	1.07
Q1127-145G1	0.328279	0.028±0.003	0.40 ^{+0.09} _{-0.07}	2.6 ^{+0.7} _{-0.4}	0.7 ^{+0.2} _{-0.1}	0.21 ^{+0.07} _{-0.06}	84 ⁺¹³ ₋₁₃	2.1 ^{+0.2} _{-0.2}	37.6 ^{+3.1} _{-4.4}	73 ⁺⁸ ₋₇	2.10	0.97
Q1127-145G2	0.328279	0.028±0.003	0.05 ^{+0.00} _{-0.00}	0.5 ^{+0.5} _{-0.3}	0.4 ^{+0.1} _{-0.1}	0.07 ^{+0.05} _{-0.04}	70 ⁺¹³ ₋₁₈	2.7 ^{+0.1} _{-0.0}	22.1 ^{+4.0} _{-2.7}	30 ⁺⁷ ₋₇	4.27	1.06
Q1148+387G1	0.553363	0.640 ± 0.013	0.07 ^{+0.02} _{-0.06}	2.9 ^{+0.6} _{-0.8}	3.3 ^{+1.1} _{-3.3}	0.06 ^{+0.05} _{-0.06}	11 ⁺¹⁷ ₋₄₈	4.1 ^{+0.2} _{-0.2}	49.8 ^{+2.2} _{-3.0}	28 ⁺² ₋₂	6.76	1.10
Q1209+107G1	0.392924	1.187±0.005	0.61 ^{+0.10} _{-0.08}	0.6 ^{+0.1} _{-0.1}	0.9 ^{+0.0} _{-0.0}	0.60 ^{+0.04} _{-0.05}	2 ⁺³ ₋₃	1.2 ^{+0.1} _{-0.3}	47.2 ^{+6.1} _{-5.1}	14 ⁺¹¹ ₋₁₉	1.21	1.21
Q1222+228G1	0.550198	0.094±0.009	0.00 ^{+0.03} _{-0.00}	2.0 ^{+0.2} _{-0.6}	1.9 ^{+0.3} _{-0.6}	0.32 ^{+0.05} _{-0.03}	48 ⁺¹³ ₋₁₈	3.3 ^{+0.2} _{-0.2}	81.3 ^{+1.0} _{-1.0}	78 ⁺¹ ₋₁	5.51	1.01
Q1241+176G1	0.550482	0.465±0.011	0.55 ^{+0.12} _{-0.10}	3.7 ^{+0.3} _{-0.6}	1.5 ^{+0.7} _{-0.4}	0.45 ^{+0.07} _{-0.05}	33 ⁺⁵ ₋₅	2.1 ^{+0.1} _{-0.2}	31.7 ^{+16.2} _{-4.8}	70 ⁺¹⁷ ₋₁₉	2.49	1.21
Q1246-057G1	0.639909	0.450 ± 0.004	0.31 ^{+0.22} _{-0.15}	0.2 ^{+0.2} _{-0.0}	5.1 ^{+0.8} _{-0.8}	0.36 ^{+0.13} _{-0.22}	20 ⁺¹³ ₋₂₆	2.7 ^{+0.4} _{-0.8}	28.6 ^{+10.5} _{-11.7}	48 ⁺⁴⁰ ₋₂₅	4.90	1.23
Q1317+277G1	0.660049	0.320±0.006	0.19 ^{+0.02} _{-0.02}	0.9 ^{+0.4} _{-0.4}	0.7 ^{+0.1} _{-0.1}	0.46 ^{+0.10} _{-0.07}	12 ⁺⁸ ₋₁₀	3.9 ^{+0.2} _{-0.2}	65.8 ^{+1.2} _{-1.2}	3 ⁺¹ ₋₁	5.11	1.12
Q1332+552G1	0.374	2.90	0.79 ^{+0.03} _{-0.03}	3.8 ^{+0.2} _{-0.2}	3.9 ^{+0.3} _{-0.2}	0.19 ^{+0.03} _{-0.02}	30 ⁺⁵ ₋₄	4.2 ^{+0.3} _{-0.3}	55.6 ^{+2.5} _{-3.0}	83 ⁺⁴ ₋₄	4.71	1.06
Q1354+195G1	0.456598	0.773 ± 0.015	0.00 ^{+0.02} _{-0.00}	2.7 ^{+0.3} _{-0.4}	5.1 ^{+1.9} _{-1.8}	0.37 ^{+0.14} _{-0.10}	27 ⁺¹³ ₋₁₀	2.4 ^{+0.1} _{-0.1}	24.7 ^{+5.7} _{-6.5}	26 ⁺¹⁴ ₋₁₄	4.04	1.06
Q1424-118G1	0.341716	0.100 ± 0.015	0.00 ^{+0.01} _{-0.00}	3.8 ^{+0.1} _{-0.0}	2.4 ^{+0.1} _{-0.3}	0.57 ^{+0.03} _{-0.02}	76 ⁺¹ ₋₂	4.6 ^{+0.1} _{-0.1}	66.2 ^{+0.5} _{-0.4}	89 ⁺¹ ₋₁	7.72	1.14
Q1511+103G1	0.4369	0.454±0.046	0.00 ^{+0.04} _{-0.00}	0.7 ^{+0.1} _{-0.2}	1.9 ^{+1.0} _{-0.3}	0.33 ^{+0.03} _{-0.04}	79 ⁺¹⁰ ₋₂₇	2.3 ^{+0.1} _{-0.1}	51.0 ^{+1.8} _{-2.2}	76 ⁺² ₋₂	3.79	1.06
Q1622+235G1	0.317597	0.491±0.010	0.64 ^{+0.02} _{-0.02}	3.1 ^{+0.1} _{-0.1}	1.0 ^{+0.1} _{-0.0}	0.31 ^{+0.03} _{-0.02}	44 ⁺² ₋₂	4.9 ^{+0.1} _{-0.2}	70.6 ^{+1.0} _{-0.8}	25 ⁺¹ ₋₁	2.20	0.95
Q1622+235G2	0.368112	0.247±0.005	0.39 ^{+0.02} _{-0.01}	4.0 ^{+0.0} _{-0.0}	3.4 ^{+0.2} _{-0.1}	0.38 ^{+0.02} _{-0.04}	35 ⁺³ ₋₃	3.4 ^{+0.0} _{-0.1}	64.2 ^{+0.7} _{-0.7}	5 ⁺¹ ₋₁	5.03	1.07
Q1622+235G3	0.471930	0.769±0.006	0.00 ^{+0.02} _{-0.00}	1.9 ^{+0.1} _{-0.1}	0.9 ^{+0.1} _{-0.2}	0.32 ^{+0.02} _{-0.02}	31 ⁺¹⁴ ₋₂₃	1.2 ^{+0.0} _{-0.0}	71.4 ^{+1.2} _{-1.2}	6 ⁺¹ ₋₁	2.02	1.07
Q1622+235G4	0.656106	1.446±0.006	0.25 ^{+0.09} _{-0.10}	0.2 ^{+0.3} _{-0.0}	3.1 ^{+0.3} _{-0.4}	0.18 ^{+0.11} _{-0.09}	41 ⁺¹⁶ ₋₁₅	3.8 ^{+0.4} _{-0.4}	65.6 ^{+2.4} _{-3.4}	3 ⁺⁴ ₋₃	4.95	1.06
Q1622+235G5	0.702902	0.032±0.003	0.03 ^{+0.01} _{-0.02}	0.4 ^{+0.1} _{-0.2}	1.2 ^{+0.4} _{-0.4}	0.69 ^{+0.01} _{-0.05}	82 ⁺¹⁶ ₋₁₈	2.9 ^{+0.1} _{-0.1}	41.7 ^{+1.5} _{-3.2}	29 ⁺³ ₋₃	4.69	1.08
Q1622+235G6	0.797078	0.468±0.008	0.95 ^{+0.05} _{-0.09}	0.5 ^{+0.0} _{-0.1}	5.8 ^{+0.2} _{-0.2}	0.58 ^{+0.02} _{-0.02}	29 ⁺² ₋₂	5.1 ^{+0.6} _{-0.8}	77.9 ^{+3.6} _{-6.2}	21 ⁺⁵ ₋₉	5.99	0.95
Q1622+235G7	0.891276	1.548±0.004	0.04 ^{+0.02} _{-0.02}	1.4 ^{+0.3} _{-0.4}	0.5 ^{+0.4} _{-0.3}	0.66 ^{+0.04} _{-0.04}	27 ⁺¹⁸ ₋₁₃	4.4 ^{+0.3} _{-0.3}	71.5 ^{+1.4} _{-1.7}	35 ⁺² ₋₁	7.19	1.15
Q1623+268G1	0.887679	0.903±0.004	0.55 ^{+0.15} _{-0.55}	0.4 ^{+0.8} _{-0.2}	7.5 ^{+1.7} _{-3.7}	0.52 ^{+0.17} _{-0.51}	73 ⁺¹¹ ₋₂₄	3.6 ^{+0.9} _{-1.4}	75.1 ^{+7.7} _{-16.3}	64 ⁺¹⁷ ₋₅	7.00	1.05
Q1623+268G2	0.887679	0.903±0.004	0.74 ^{+0.16} _{-0.21}	3.7 ^{+0.3} _{-0.8}	2.0 ^{+0.3} _{-0.3}	0.57 ^{+0.13} _{-0.18}	64 ⁺¹⁸ ₋₁₂	1.5 ^{+0.7} _{-0.4}	74.2 ^{+10.8} _{-12.8}	78 ⁺¹¹ ₋₁₂	2.25	1.10
Q2128-123G1	0.429735	0.395±0.010	0.07 ^{+0.04} _{-0.03}	3.5 ^{+0.5} _{-0.7}	1.6 ^{+1.5} _{-0.7}	0.56 ^{+0.14} _{-0.12}	33 ⁺¹⁹ ₋₁₉	2.9 ^{+0.2} _{-0.2}	48.3 ^{+3.5} _{-3.7}	75 ⁺⁶ ₋₅	4.65	0.96
Q2206-199G1	0.948361	0.249 ± 0.002	0.64 ^{+0.10} _{-0.13}	3.1 ^{+0.4} _{-0.5}	1.9 ^{+0.2} _{-0.2}	0.47 ^{+0.07} _{-0.09}	11 ⁺⁷ ₋₉	2.2 ^{+0.4} _{-0.3}	73.2 ^{+3.9} _{-4.5}	23 ⁺⁷ ₋₄	2.59	1.01
Q2206-199G2	1.017038	1.047 ± 0.003	1.00 ^{+0.00} _{-0.05}	0.5 ^{+0.0} _{-0.0}	9.5 ^{+0.4} _{-0.4}	0.07 ^{+0.04} _{-0.04}	82 ⁺¹² ₋₁₈	22.3 ^{+1.8} _{-1.8}	2.9 ^{+17.4} _{-2.9}	70 ⁺²⁰ ₋₅₅	9.62	1.65

els do not include degrees of freedom to fit spiral arms, HII regions etc. seen in some galaxy images. For example, one can clearly see these structures in the residual images of Q0229+131G1 (spiral arms) and Q0454–220G1 (HII regions).

In Table 5 we list the galaxy morphological properties extracted from the GIM2D models. The 40 galaxies have a mean disk scale length of 3.8 kpc, which is larger than the estimated value for the Milky Way of 2.3 ± 0.6 kpc (Hammer et al. 2007). The sample mean bulge scale length is 2.5 kpc, which is comparable to estimates of the Milky Way bulge of 2 kpc (Rich 1998). The average Sérsic index for the sample is $\langle n \rangle = 1.9$. We find 23 galaxies having well-modeled disk-like bulges with Sérsic indices of $n < 2$ and 17 galaxies having steeper bulge profiles with $n \geq 2$.

3.1.1 MgII Absorbers Compared to DEEP Galaxies

In order to determine if MgII absorption-selected galaxies differ from field galaxies, we compare the bulge and disk size distribution from our sample to galaxies having similar properties obtained from the Deep Extragalactic Exploratory Probe (DEEP) Groth Strip Galaxy Redshift Survey (see Simard et al. 2002; Vogt et al. 2005; Weiner et al. 2005). Simard et al. (2002) used GIM2D to model WFPC-2/HST F606W and 814W images of 7450 galaxies from the DEEP survey. We selected a subset of 429 galaxies that have both a redshift and magnitude range similar to those represented by our sample (see Table 3). The mean redshift for the 429 DEEP galaxies is $\langle z \rangle = 0.68$, peaking at $z \sim 0.9$. In Figure 4c we show the redshift distribution for our sample having a mean redshift of $\langle z \rangle = 0.51$, peaking at $z \sim 0.4$. Since the redshift distributions for the two samples are quite different, we used our redshift distribution as a selection function to randomly select a subset of the 429 DEEP galaxies to make a fair comparison. We randomly selected 120 DEEP galaxies that reproduce the redshift distribution of our sample seen in Figure 4c. We produced several DEEP sub-samples all resulting in the similar distributions of bulge effective radii and disk scale lengths.

The galaxies from the DEEP sample were fit using GIM2D where the bulge Sérsic index is limited to $n = 4$, whereas we allowed the bulge Sérsic index to vary between $0.2 \leq n \leq 4.0$ for our galaxy model fits. In order to make a direct comparison with the DEEP galaxies, we refit our 40 galaxies with a fixed Sérsic index of $n = 4$. It is also worth noting that the majority of our galaxies were observed using the WFPC-2 F702W filter, whereas the DEEP survey used two different WFPC-2 filters; a bluer F606W filter and a redder F814W filter. The model fits to the DEEP F606W and F814W images produce similar size distributions (see Fig 4a,b). Given that our galaxy images were taken primarily using a filter with a central wavelength between the central wavelength of the two filters used in DEEP, we do not expect that the difference in filter band-pass used will produce any shifts/differences in the disk and bulge size distributions.

In Figure 4a, we show the normalized distribution of bulge effective radii averaged over several random sub-samples of 120 galaxies derived from the DEEP F606W images, the DEEP F814W images, our sample of 40 galaxies having free Sérsic index fit, and our sample fit with $n = 4$. The mean values along with the mean fit errors are shown. For our sample, the mean value is consistent with those derived from the DEEP sample, although more galaxies are found with smaller bulge effective radii in the latter. The K-S probability that the DEEP sample and our sample (fit with $n = 4$) are drawn from the same population is $P(KS) = 0.27$, which suggests that the two distributions are similar and only differ at 85%

c.l. (1.11σ). Note that for our sample, when the Sérsic index is fixed at $n = 4$, the bulge sizes tend to increase on average. As the bulge contribution increases, it is reflected as a smaller size distribution of the galaxy disks as seen in Figure 4b.

In Figure 4b, we show the disk scale length distribution. Here we find that the averaged sub-samples of 120 DEEP galaxies have a lower mean r_d than found for our sample. On average, our sample has more galaxies with larger r_d compared to those from the DEEP survey. The K-S probability that the DEEP sample and our sample (fit with $n = 4$) are drawn from the same distribution is $P(KS) = 0.27$, which suggests that the two distributions are similar and only differ at the 73% c.l. (1.11σ). However, if we compare our sample, when using a free Sérsic index fit, this increases to 3.7σ and the mean value is now inconsistent with those of the DEEP survey.

We find our sample, when fit with $n = 4$, similar to the galaxies in the DEEP sample: differences arise only when we have a free index fit. This difference is only due to the fitting and not a physical difference.

3.2 Galaxy Type and Absorption

It is difficult to classify the morphological type (i.e., E4, Sb, etc) of a galaxy using only the quantified morphological parameters presented here. While early-type galaxies are expected to have high Sérsic indices of $n \geq 2$, over 25% of spirals have bulges with $n > 2$ (see Weinzirl et al. 2009). Thus, the Sérsic index is not ideal for classifying galaxy morphology. Instead we have used the bulge-to-total ratio to separate early-type ($B/T > 0.5$) and late-type galaxies ($B/T < 0.5$). We expect less than 8% (± 3 galaxies) contamination by applying a $B/T = 0.5$ cutoff (Weinzirl et al. 2009).

For our sample, we find 27 late-type galaxies and 13 early-type galaxies; these numbers are consistent with the distribution of galaxy morphologies found in the field environment (van den Bergh 2004; Hammer et al. 2005, 2009). In Figure 5a, we show the distribution of galaxy type as a function of $W_r(2796)$. The mean $W_r(2796)$ for the early-type galaxies is 1.0 \AA and is slightly lower for late-type galaxies at 0.7 \AA ; both types are accompanied by a large spread in equivalent width.

In Figure 5b, we show the $W_r(2796)$ as a function of impact parameter, where red points are early-type galaxies and blue points are late-type galaxies. The mean impact parameter for each morphology type is the same: 57 kpc. There are some interesting trends to note. For $D \leq 40$ kpc, we find a higher proportion of late-type galaxies (12/15) that span a large equivalent width range. Beyond 40 kpc, we find more of a mixture of early and late-types, with late-type galaxies dominating (14/25). In this impact parameter regime, we also see that late-type galaxies tend to have weaker absorption than early-types. The data suggests that late-type galaxies are the dominate galaxy type selected by MgII absorption at all impact parameters. We note that Chen et al. (2010a) also find more spirals in close proximity to the quasar line of sight and find a factor of two more early-type galaxies at higher impact parameters ($D > 43$ kpc). A K-S test yields that the equivalent width distributions of the late-type and early-type galaxies in our sample differ by 2.1σ . Given the low number statistics of our sample and the larger scatter of $W_r(2796)$ associated with late-type galaxies, we caution any against any definitive conclusions being drawn from Figure 5.

It could be possible that the physical scale lengths, i.e., r_d , r_h , r_b , etc., of a galaxy may be related to its halo gas absorption properties. Having quantified the morphological parameters of the galaxies in our sample, we have applied generalized Kendall and Spearman rank correlation tests, which accounts for measured limits in

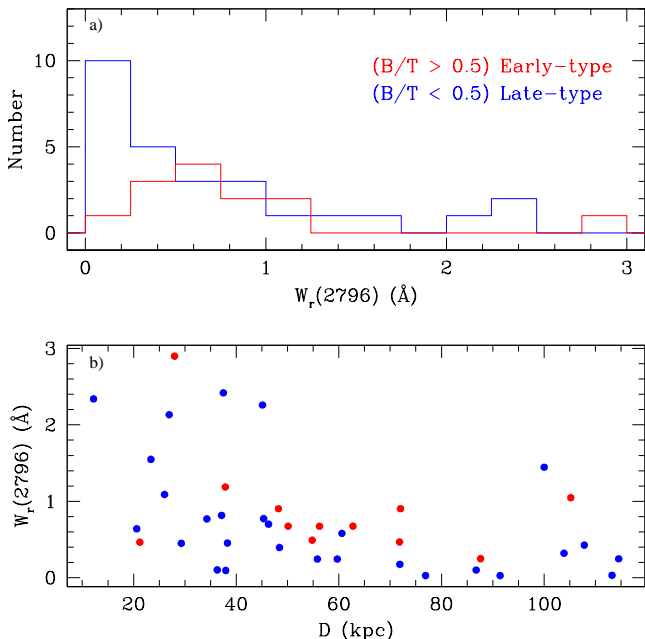


Figure 5. — (a) The distribution of the Mg II $\lambda 2796$ rest-frame equivalent width, $W_r(2796)$, as a function of galaxy morphology. Galaxies have been separated into to classes using the bulge-to-total ratio: late-type ($B/T > 0.5$) and early-type ($B/T < 0.5$). Note that a large fraction of late-type galaxies are associated with low equivalent width systems. — (b) The impact parameter as a function of the $W_r(2796)$ is shown for all 40 galaxies in our sample. The blue points are late-type galaxies and the red points are early-type galaxies. We find a 3.2σ anti-correlation. Note the large scatter in the correlation and the lack for high D galaxies with high $W_r(2796)$.

the sample (Feigelson & Nelson 1985), between the galaxy scale lengths, Sérsic index, n , and bulge-to-total ratio, B/T and the measured absorption properties. We find no evidence for trends with these morphological parameters (all significance levels are less than 2σ). This may suggest that galaxy mass, size, and/or global stellar distribution is/are not important factor(s) in dictating the absorption properties of gaseous halos.

3.3 Impact Parameter and Absorption

For many studies an anti-correlation between $W_r(2796)$ and D has been noted and employed to understand the geometry, mean radial density profile, and cross-sectional covering fraction of Mg II halo gas (e.g., Lanzetta & Bowen 1990; Steidel 1995; Churchill, Steidel, & Vogt 1996; Mo & Miralda-Escude 1996; Bouché et al. 2006; Chelouche et al. 2008; Chen & Tinker 2008; Chen et al. 2010a; Steidel et al. 2010). For our sample, we find a 3.2σ anti-correlation (see Figure 5b). Though it is clear that projected galactocentric distance is a predominant parameter governing absorption strength, there is significant scatter in the relation, showing that distance from the host galaxy may not be the only physical parameter governing the distribution and observed quantity of halo gas. For example, at various levels of influence, star formation rate, environment, or the orientation of the line of sight (galaxy inclination and/or position angle relative to the quasar) could also play a role.

As a caveat with regards to interpreting this anti-correlation,

we note that, given the classical methods used to identify host galaxies (find absorption then search for host galaxy), our sample and previous samples are relatively biased toward galaxies in close proximity to the quasar, which may artificially lead to the observed anti-correlation. As unbiased surveys (e.g., Tripp & Bowen 2005; Barton & Cooke 2009) are enlarged, we will be able to obtain more robust data to examine the significance of the D and $W_r(2796)$ anti-correlation. Taken at face value, the observed anti-correlation between $W_r(2796)$ and D would suggest that either the column density and/or velocity spread of the absorbing gas decreases with galactocentric distance.

In Table 6, we present the results of additional correlation tests between the absorption properties and D . What is immediately clear is that *all* our measures of the gas absorption strength decrease with D , although we note that the doublet ratio increases with D as expected. $W_r(2803)$, which is less sensitive to saturation than is $W_r(2796)$, anti-correlates significantly with D . Though N_{cl} , N_{vp} and τ do not show a significant anti-correlation with D , they do follow the trend of decreasing with D . Taken together, the anti-correlation trends show a consistent signature that, on average, Mg II absorbing gas becomes optically thinner with increasing projected galactocentric distance from the host galaxy.

As stated above, the decreasing equivalent widths indicate that either the column density and/or velocity spread of the absorbing gas decreases with galactocentric distance. However, the facts that (1) $W_r(2803)$ shows a slightly higher significance than $W_r(2796)$, (2) the doublet ratio increases with D , and (3) the mean velocity, W_{vs} , and the velocity asymmetry, A , scatters with D (shows no signature of decreasing with D), together suggest that a decrease in column density with D , rather than just a decrease in velocity structure, is likely the dominant behavior of the halo gas.

3.4 Galaxy Color and Absorption

Given the results of Zibetti et al. (2007), who statistically show that larger $W_r(2796)$ is associated with bluer galaxies, and the results of Ménard et al. (2009), who find a highly significant correlation between [O II] luminosity and $W_r(2796)$, we might expect to find that bluer galaxies in our sample are associated with larger $W_r(2796)$. We thus tested for a correlations between $B - K$ galaxy color and absorption properties in our sample.

At the range of significance level $\sim 2-2.2\sigma$, dominated by N_{cl} , N_{vp} , and $\langle V \rangle$, we find larger absorption quantities tend to be associated with the bluer galaxies. The Spearman Kendall results are presented in Table 6. If we were to interpret these trends, we would infer that redder (early-type) galaxies are associated with low column density absorption with fewer kinematic components than bluer (late-type) galaxies. We do not find evidence supporting a trend of increasing $W_r(2796)$ with decreasing $B - K$, as found by Zibetti et al. (2007).

The result for our sample is consistent with the results of Chen et al. (2010a), who examined a sample of 71 systems. They find no significant correlation between $B - R$ galaxy color and $W_r(2796)$. It remains difficult to directly compare our work and the work of Chen et al. because the works employ different colors. It is also difficult to compare our work to those of Zibetti et al. due to the stacking nature of their data analysis, the difference in the $W_r(2796)$ distribution of the two samples, and the use of different colors in both samples. We further discuss these samples and their results in Section 4.

Table 6. Selected results of the Kendall and Spearman rank correlation tests between the Mg II absorption properties and the associated galaxy properties. In column (1) are the tested properties and (2) has the number of systems tested. In columns (3)–(5) are the Spearman correlation coefficient, r_s , the probability, P_S , that the tested data are consistent with the null hypothesis of no correlation, and the number of standard deviations, N_{Sor} where the ranks are drawn from a normal distribution. In columns (6)–(8) are the Kendall τ_K , the probability, P_K , and N_{Kor} .

Tests	Galaxies	r_s	P_S	N_{Sor}	τ_K	P_K	N_{Kor}
D vs. $W_r(2803)$	40	-0.51	0.0015	3.18	-0.73	0.0010	3.30
D vs. $W_r(2796)$	40	-0.49	0.0022	3.06	-0.70	0.0014	3.19
D vs. DR	40	0.37	0.0219	2.29	0.51	0.0210	2.31
D vs. N_{cl}	34	-0.33	0.0578	1.90	-0.46	0.0503	1.96
D vs. N_{vp}	34	-0.32	0.0644	1.85	-0.43	0.0752	1.78
D vs. W_{vs}	34	-0.28	0.1038	1.63	-0.35	0.1461	1.45
D vs. τ	34	-0.22	0.2082	1.26	-0.29	0.1492	1.44
D vs. N_a	34	-0.14	0.4202	0.81	-0.21	0.3076	1.02
D vs. $\langle V \rangle$	34	-0.08	0.6361	0.47	-0.11	0.6351	0.48
D vs. A	34	0.01	0.9783	0.03	-0.03	0.9056	0.12
<hr/>							
$B - K$ vs. N_{cl}	23	-0.47	0.0272	2.21	-0.66	0.0251	2.24
$B - K$ vs. N_{vp}	23	-0.49	0.0207	2.31	-0.65	0.0301	2.17
$B - K$ vs. $\langle V \rangle$	23	0.41	0.0554	1.92	0.63	0.0344	2.12
$B - K$ vs. W_{vs}	23	-0.33	0.1218	1.55	-0.52	0.0809	1.75
$B - K$ vs. $W_r(2796)$	27	-0.31	0.1156	1.57	-0.45	0.0991	1.65
$B - K$ vs. A	23	0.36	0.0963	1.66	0.47	0.1125	1.59
$B - K$ vs. τ	23	-0.33	0.1248	1.54	-0.37	0.1489	1.44
$B - K$ vs. $W_r(2803)$	27	-0.29	0.1423	1.47	-0.37	0.1749	1.36
$B - K$ vs. DR	27	0.24	0.2139	1.24	0.35	0.2030	1.27
$B - K$ vs. N_a	23	-0.21	0.3214	0.99	-0.23	0.3731	0.89
<hr/>							
M_B vs. N_a	34	0.20	0.2523	1.15	0.26	0.2292	1.20
M_B vs. A	34	-0.19	0.2791	1.08	-0.24	0.3277	0.98
M_B vs. DR	40	0.13	0.4211	0.81	0.20	0.3633	0.91
M_B vs. W_{vs}	34	-0.15	0.3795	0.88	-0.21	0.3736	0.89
M_B vs. N_{cl}	34	-0.13	0.4639	0.73	-0.18	0.4515	0.75
M_B vs. τ	34	0.12	0.4774	0.71	0.16	0.4625	0.74
M_B vs. $\langle V \rangle$	34	0.08	0.6487	0.46	0.11	0.6564	0.45
M_B vs. $W_r(2796)$	40	-0.08	0.6222	0.49	-0.09	0.6919	0.40
M_B vs. N_{vp}	34	0.05	0.7700	0.29	0.09	0.6998	0.39
M_B vs. $W_r(2803)$	40	-0.08	0.6246	0.49	-0.07	0.7354	0.34
<hr/>							
i vs. N_{cl}	34	0.38	0.0297	2.17	0.52	0.0279	2.20
i vs. N_a	34	0.36	0.0389	2.07	0.48	0.0292	2.18
i vs. N_{vp}	34	0.34	0.0546	1.92	0.51	0.0327	2.14
i vs. τ	34	0.31	0.0790	1.76	0.40	0.0729	1.79
i vs. $W_r(2796)$	40	0.24	0.1318	1.51	0.33	0.1358	1.49
i vs. A	34	-0.31	0.0799	1.75	-0.36	0.1381	1.48
i vs. $W_r(2803)$	40	0.19	0.2251	1.21	0.28	0.2039	1.27
i vs. W_{vs}	34	0.20	0.2412	1.17	0.28	0.2474	1.16
i vs. $\langle V \rangle$	34	-0.05	0.7794	0.28	-0.07	0.7668	0.30
i vs. DR	40	-0.04	0.8161	0.23	-0.04	0.8521	0.17
<hr/>							
i/D vs. $W_r(2796)$	39	0.63	9.24×10^{-5}	3.91	0.97	1.40×10^{-5}	4.34
i/D vs. $W_r(2803)$	39	0.63	0.0001	3.88	0.96	1.84×10^{-5}	4.28
i/D vs. N_a	33	0.65	0.0002	3.70	0.93	3.79×10^{-5}	4.12
i/D vs. τ	33	0.61	0.0006	3.44	0.87	0.0001	3.86
i/D vs. N_{cl}	33	0.58	0.0010	3.30	0.85	0.0004	3.54
i/D vs. N_{vp}	33	0.53	0.0029	2.98	0.78	0.0015	3.18
i/D vs. DR	39	-0.41	0.0115	2.53	-0.58	0.0093	2.60
i/D vs. W_{vs}	33	0.40	0.0234	2.27	0.56	0.0227	2.28
i/D vs. A	33	-0.08	0.6357	0.47	-0.13	0.6090	0.51
i/D vs. $\langle V \rangle$	33	0.03	0.8552	0.18	-0.01	0.9629	0.05

3.5 Galaxy Luminosity and Absorption

A Holmberg-like luminosity scaling of the radius of MgII absorbing halo sizes has been discussed at length in the literature (Steidel 1995; Chen & Tinker 2008; Kacprzak et al. 2008; Chen et al. 2010a). For the sample of galaxies presented here, Kacprzak et al. (2008) showed that the MgII absorption halo size exhibits a scaling with the galaxy luminosity (albeit not with a clean cut-off size). Do the absorption properties also exhibit a scaling with luminosity? To investigate this question, we examined if there is a correlation between absorption properties and M_B (effectively the galaxy luminosity). We find no evidence of a correlation with M_B for any the absorption properties. The Spearman and Kendall results are presented in Table 6. This would suggest that galaxy luminosity is not a predominant governing factor in determining the absorption strength, optical thickness, or velocity spread of the MgII gas in our sample.

3.6 Galaxy Orientation and Absorption

Lanzetta & Bowen (1992) and Charlton & Churchill (1996) showed that if there are preferred systematic kinematics and spatial distributions of MgII absorbing gas relative to the host galaxies, then the absorption strengths and kinematics would be expected to follow a predictable behavior as a function of galaxy orientation and impact parameter. By orientation, we refer to the galaxy inclination, i , and the position of the quasar line of sight relative to the major axis of the galaxy, θ , which ranges from $\theta = 90^\circ$ when the quasar aligns with the major galaxy axis to $\theta = 0^\circ$ when the quasar aligns with the galaxy minor axis.

Charlton & Churchill (1996) further demonstrated that MgII halos could be disk-like since, statistically, the MgII redshift path density could be satisfactorily explained by extended disks as well as by spherical halos. They predicted that if absorbers are disk-like in origin, then (1) the mean $W_r(2796)$ for a given inclination increases with i , (2) the relative number of stronger absorbers peaks when the quasar probes the major axis ($\theta = 0^\circ$), and (3) the mean ratio of the absorption kinematic spread to the Tully Fisher velocity of the galaxy increases with i . Making a direct comparison of galaxy and MgII absorption kinematics, Steidel et al. (2002) showed that galaxy halos are partially understood by lagging disk-like kinematics. Binning MgII absorption profiles by inclination, Kacprzak et al. (2010a) found that the mean optical depth and mean velocity spread of the absorbing gas was larger for higher inclination galaxies.

From the above predictions, if flattened halos that are co-planar with the galaxy disk dominate, we expect the absorption properties to correlate with inclination and anti-correlate with position angle (be strongest at $i = 90^\circ$ and $\theta = 0^\circ$). On the other hand, it is also possible that star-formation driven winds could be a dominant source of observed MgII absorption (especially for the stronger absorbers, e.g., Zibetti et al. 2007; Weiner et al. 2009). In contrast to AGN driven winds, star-formation driven winds are spatially distributed geometrically perpendicular to the plane of the galaxy (see Veilleux et al. 2005). Thus, for winds, we would expect the absorption properties and velocity widths to be anti-correlated with inclination and correlate with position angle (be strongest at $i = 0^\circ$ and $\theta = 90^\circ$). In reality, both scenarios, possibly further complicated by additional scenarios such as mergers, IGM filament accretion, etc., contribute to the presence of MgII absorption. Are the predicted observational signatures of one of these scenarios man-

ifest in the data, which would suggest predominance of the scenario?

GIM2D yields two position angles – one for the bulge and one for the disk. We employ the bulge-to-total ratio for adopting the best representative galaxy position angle, such that when $B/T > 0.5$ we use bulge, θ_b , and when $B/T < 0.5$ we use the disk, θ_d . For our sample, we find that the distribution of inclinations and position angles of galaxies selected by MgII absorption are not inconsistent with having been drawn from a population of field galaxies (for which the distribution of inclinations is $\propto \sin^2 i$ and position angles are random). A K-S test for the inclination distribution yields a K-S statistic of 0.16 and $P(KS) = 0.27$ and for the position angle distribution yields 0.16 with $P(KS) = 0.28$. At face value, this would suggest that galaxies chosen by known absorption are distributed on the sky no differently than galaxies selected at random. This might further suggest that halos have a uniform spatial distribution around their host galaxies. However, there is a wide range of absorption properties (which are governed by the column densities and kinematics, i.e., velocity widths) and the overall distribution of orientations relative to the line of sight cannot, by themselves, discriminate whether absorption properties vary in a systematic fashion with orientation.

We find no correlation between θ and any of absorption properties (the highest significance is 1.4σ); the absorption properties are consistent with a random distribution as a function of position angle (these results are independent of our B/T selection criteria).

The results of correlation tests between the absorption properties and inclination i are similar to the tests with impact parameter; we find several trends toward a correlation above the 2.0σ level. The Spearman and Kendall quantities are presented in Table 6. The strongest trends are N_{cl} , N_a , and N_{vp} all showing that these quantities tend to increase with increasing inclination. Taken together, these trends could suggest a *potential* correlation between disk inclination and the column density, number of clouds, and $W_r(2796)$.

Overall, these results are suggestive (not definitive) that the observational signature from the predictions of a co-planar geometric model dominate over the other plausible scenarios for the origin and location of the absorbing gas. They are consistent with the findings of Kacprzak et al. (2010a) that the optical depth and velocity spread of the gas, relative to the galaxy systemic velocity, increases with disk inclination. Interestingly, we do not find a trend suggested by Charlton & Churchill (1996) for increasing W_{vs} (normalized by the Tully Fisher velocity, computed from L_B) with increasing inclination (0.2σ). A simple galaxy disk model is not supported by the position angle data, which are not necessarily consistent with the co-planar geometry scenario. If the absorbing gas were in a disk, then the radial distance out on the disk mid-plane probed by the line of sight is given by $r = D \sqrt{1 + \tan^2 i \sin^2 \theta}$. Correlation tests between the absorption properties and r might be expected to have higher significance (less scatter) than those with D (even allowing for all disks not being equal). For our sample, the absorption properties exhibit uncorrelated scatter with r (no test had a significance above 2σ). Thus, at best, we find the data suggestive that most MgII absorbers have a co-planar geometry, but are not necessarily disks (also see the geometric and kinematic models of Kacprzak et al. 2010a). Since there is a substantial scatter in the absorption properties, there is some difficulty in interpreting these trends. Since the distribution of inclinations for our sample is consistent with that of a random sample of galaxies, our sample has a larger number of higher inclination galaxies than lower inclination galaxies [18/40 galaxies have $i > 60^\circ$ and only 5/22 have $i < 30^\circ$]. With a paucity

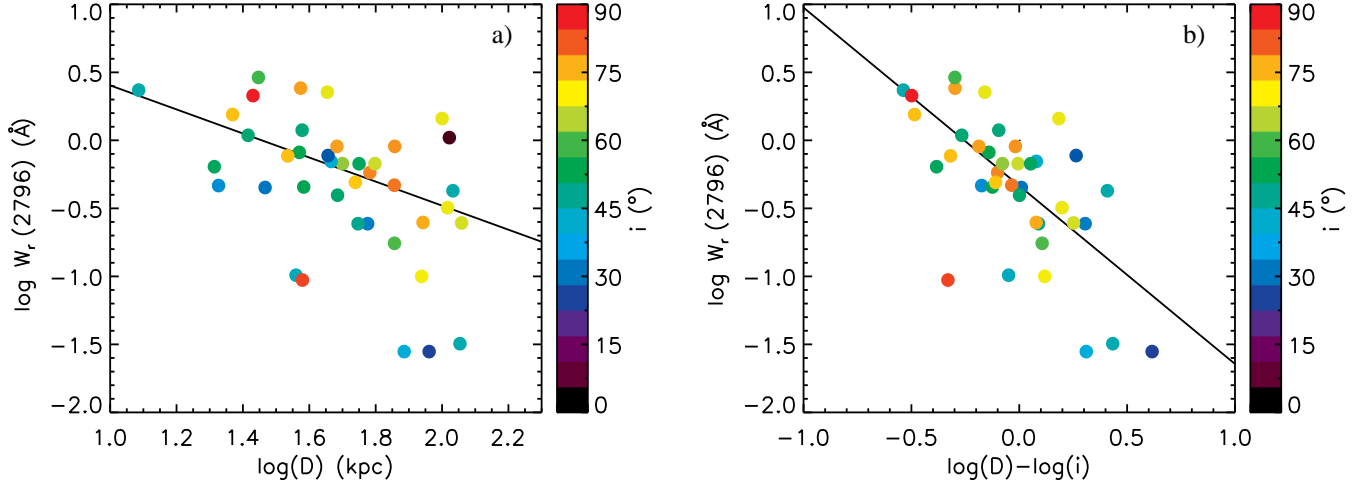


Figure 6. — (a) The 3.2σ anti-correlation between $W_r(2796)$ and impact parameter D . Note the large scatter in the correlation. The dark line shows a maximum-likelihood fit to the data with $\log(W_r(2796)) = 1.228 - 0.884\log(D)$. The points are color-coded as a function of galaxy inclination angle, i . It is apparent that galaxies with high, mid, and low inclinations populate different regions of the plot. For a fixed D , high inclination galaxies tend to have higher $W_r(2796)$ than low inclination galaxies. This inclination gradient in the $W_r(2796)$ direction suggests that inclination plays a secondary but significant role in determining the $W_r(2796)$ of an absorption system. — (b) A correction for inclination is applied to the $W_r(2796)$ and D anti-correlation. The scatter is now reduced and results in a 4.3σ correlation between $W_r(2796)$ and i/D . Note the different inclinations are now overlapping compared to (a). The dark line shows a maximum-likelihood fit to the data with $\log(W_r(2796)) = -0.334 - 1.310\log(D/i)$.

of low inclination (predominantly face on) galaxies, any possible scatter in the absorption properties for low inclination may not be well represented in our sample. However, there is no clear or evident bias in our sample that could explain why the lower inclination galaxies have lower strength absorption properties.

3.7 Normalization by Impact Parameter

As discussed in Section 3.3, the anti-correlations between $W_r(2796)$ and D and between $W_r(2803)$ and D , and decreasing trends with the remaining absorption properties, all corroborate a physical picture in which the column densities diminish with increasing D . This suggests that impact parameter has a strong influence on the absorption properties and that calibrating out impact parameter for the correlation tests between galaxy properties and absorption properties may uncover otherwise diluted physically motivated trends or correlations. From the point of view of non-parametric rank correlation estimators, multiplying the absorption properties by D is equivalent to dividing the galaxy properties by D . We adopt the latter approach. Since one of the strongest indicators of a dependence of the absorption on the galaxy properties is orientation, we focused on the galaxy inclination.^{6,7}

Following normalization of i by D , we find that N_{vp} , N_{cl} , τ , N_a , $W_r(2803)$, and $W_r(2796)$ are all correlated with the normalized inclination, i/D , at a greater than 3.2σ significance. The strongest correlation is between $W_r(2796)$ and i/D , which has a one part in 10^5 probability of being consistent with no correlation (4.3σ). The

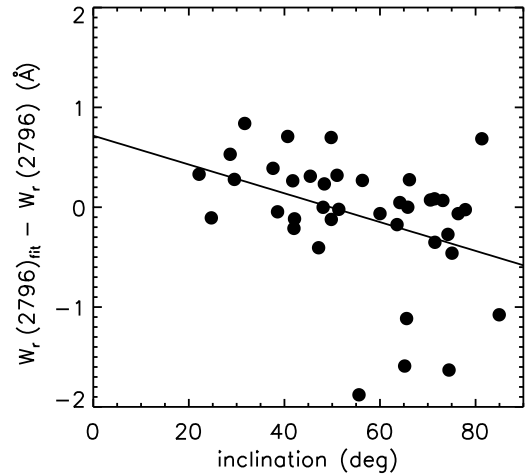


Figure 7. The galaxy inclination as a function of the equivalent width residuals computed from the fit between $W_r(2796)$ versus D (Figure 6a). We find a 2.6σ correlation between the residuals (scatter) and the galaxy inclination. This correlation further demonstrates the significance in the reduction of scatter between $W_r(2796)$ versus D when galaxy inclination is taken into account.

results are presented in Table 6. We note that D does not appear to correlate with i (only at 1.5σ).

In Figure 6a, we show the 3.2σ anti-correlation between $W_r(2796)$ and D . As we have discussed in Section 3.3, there is large scatter observed in the $W_r(2796)$ and D anti-correlation. In Figure 6a, we also color-code the data points as a function of galaxy inclination. It is clearly noticeable that high, mid, and low galaxy inclinations populate different regions of the plot and are offset from each other as a function of $W_r(2796)$ (i.e., for a fixed D , high inclination galaxies tend to have higher $W_r(2796)$ than low inclination galaxies). The galaxy inclination gradient in the $W_r(2796)$ direc-

⁶ We performed the correlation tests on all galaxy properties, but find that, unless discussed in the text, there were no other statistically significant (i.e., greater than 3σ) correlations when normalizing by D .

⁷ We have removed galaxy Q2206-199G2 from the rank correlation tests when normalizing by D because its value of inclination and errors, $i = 2.9^{+17.4}_{-2.9}$ and $D = 105.2$ kpc, provides no constraints on the ratio of $\log(D/i)$.

tion suggests that inclination plays a secondary role but significant determining the $W_r(2796)$ of an absorption system.

In Figure 6b, we apply a galaxy inclination correction. We note that our discussions of rank correlation tests are in terms of the galaxy inclination normalized by the impact parameter, i/D , however, in Figure 6b we chose to plot D/i in order to aid the reader to directly compare the scatter from both panels. Note that the scatter is significantly reduced and that there is now no clear inclination gradient seen in the distribution of data. A maximum-likelihood fit to the $W_r(2796)$ and i/D correlation is provided in Table 7. In Figure 7 we show that if we fit the anti-correlation between $W_r(2796)$ versus D (Figure 6a), then the equivalent width residuals computed from the fit correlate with galaxy inclination at 2.6σ , further supporting the significance in the reduction of scatter in Figure 6b.

We also apply bootstrap statistics to test the probability that a random distribution of inclination values could produce the inclination gradient as a function of $W_r(2796)$ seen in Figure 6a, which results in the tightening of the anti-correlation seen in Figure 6b. We used our 40 data points of $W_r(2796)$ and D pairs since they exhibit the expected correlation shown in Figure 6a. We then took our measured values of i and randomly reassigned them to the $W_r(2796)$ and D pairs, thereby creating a new bootstrap realization of the sample. We then repeated this process 1×10^6 times and computed the Kendall rank correlation test for each realization of the sample. We find that the probability of this correlation occurring by chance due to random selection of galaxy inclinations is $P = 0.00040$. Thus, it is unlikely that this correlation is due to random chance at the 3.54σ significance level.

Thus, we find that the distribution of halo gas absorption strengths has both an impact parameter *and* inclination dependence, which suggests that the gas in the halo is not spherically distributed. That is, these results suggest that MgII halo gas has a co-planar geometry and is coupled to the inclination of the galaxy disk. The correlation is opposite to that expected for wind models.

We also examined if multiples of the galaxy bulge and disk scale lengths, D/r_b and D/r_d , and half-light radii, r_h , might further reduce the scatter in the above correlations by using the quantities $i/(D/r_d)$, etc. However, we found that multiples of the scale lengths resulted in greater scatter and no statistically significant correlations with absorption properties. We also normalized the galaxy position angle by D and re-examine the scatter in the absorption properties with θ . We found a slight increase in the significance levels from 1.4σ and below to $\approx 3.0\sigma$ and below. However, these significance levels remain lower than the significance level of the anti-correlation between $W_r(2796)$ and D . As such, the increased significance levels are primarily driven by the normalization of D . The upshot is that, if the selection of galaxies by MgII absorption yields a preferred position angle–impact parameter range in relation to the absorption strength properties, it has a much larger scatter than does the preferred inclination–impact parameter range for a given range of absorption properties.

4 DISCUSSION

Several studies have shown that the morphologies of intermediate redshift ($0.3 < z < 1.0$) MgII absorption-selected galaxies appear to be qualitatively similar to those of “typical” local field galaxies (Steidel 1998; Chen et al. 2001; Chen & Lanzetta 2003; Kacprzak et al. 2007). Using GIM2D to quantify the morphological parameters of $0.3 < z < 1.0$ MgII absorption-selected galaxies, we find that their bulge and disk size distributions are also similar to

those found for field galaxies at similar redshift. Our results quantitatively show that galaxies selected by MgII absorption are, broadly speaking, “typical” galaxies. Nevertheless Kacprzak et al. (2007) has shown that MgII absorption-selected galaxies appear to have higher morphological asymmetries than field galaxies. If the latter is true, then accurately modeling absorption-selected galaxies with smooth light profiles may be more difficult given their higher level of morphological asymmetries. The difficulties may induce more scatter in the distribution of morphological parameters thereby potentially mitigating the significance levels of any correlations between galaxy properties and absorption properties.

It remains strongly debated whether MgII absorption systems arise from star formation driven winds or an array of structures such as tidal streams, satellites, filaments, etc. Here we argue that our sample of galaxies, 75% of which have $W_r(2796) < 1.0 \text{ \AA}$, does not support a scenario in which winds are the predominant mechanism producing the absorption. Overall, it is likely that an admixture of these processes contribute to the observed MgII absorption systems; below, we will argue that winds may dominate the high equivalent width regime, whereas other processes dominate the lower equivalent width regime.

For reference, in Table 7 we list the known quantified correlations between the MgII absorption properties and the host galaxy properties, which we will be discussing in the remainder of this section. The $W_r(2796)$ range used in each study is also listed.

Studies of strong MgII systems (i.e., $W_r(2796) \gtrsim 1 \text{ \AA}$), where host galaxies typically have $D \lesssim 25 \text{ kpc}$, have shown that they are likely produced by winds from high star-forming galaxies (e.g., Prochter et al. 2006). Bouché et al. (2006) report an anti-correlation between $W_r(2796)$ and the amplitude of the cross-correlation between luminous red galaxies (LRGs) and MgII absorbers (also see Gauthier et al. 2009; Lundgren et al. 2009). They conclude that stronger absorption systems are not produced by virialized gas within galaxy halos but that they originate in supernovae-driven winds. The Bouché et al. results are consistent with those of Zibetti et al. (2007), who find that stronger absorption systems with $W_r(2796) \gtrsim 1.2 \text{ \AA}$ are associated with blue star-forming galaxies. Ménard et al. (2009) showed that for stronger systems, $W_r(2796)$ correlates with the associated [OII] luminosity, an estimator of star formation rates (also see Noterdaeme et al. 2010). In a detailed study of two ultra-strong MgII absorption systems, with $W_r(2796) > 3.6 \text{ \AA}$, Nestor et al. (2010) reported nearby galaxies with star formation rates exceeding $\sim 10\text{--}90 \text{ M}_\odot \text{ yr}^{-1}$ (also see Nestor et al. 2007). These results support the idea that winds produced by star-forming regions and/or supernovae are responsible for a large proportion of the strong absorption systems ($\gtrsim 1 \text{ \AA}$) detected in the halos of galaxies.

Our study, and others (e.g., Churchill, Steidel, & Vogt 1996; Churchill & Vogt 2001; Steidel et al. 2002; Churchill, Vogt, & Charlton 2001; Chen & Tinker 2008; Chen et al. 2010a,b; Kacprzak et al. 2010a), use higher resolution spectra that are sensitive to lower equivalent widths. The general conclusions from these moderate-to-low equivalent width studies all point to other sources for producing the observed MgII absorption.

Using a similar sample to the one presented here, Kacprzak et al. (2007) found a correlation between galaxy asymmetry, normalized by D , and $W_r(2796)$ suggesting that galaxy minor mergers and harassments may be producing the absorption detected in halos. Their correlation strengthens when $W_r(2796) \geq 1.4 \text{ \AA}$ systems were removed, suggesting that interactions (or processes that gently perturb galaxy morphology) may dominate the

Table 7. Currently known quantified correlations between the Mg II absorption properties and the host galaxy properties: (1) The correlation between $W_r(2796)$ and galaxy inclination normalized by impact parameter, i/D ; (2) The anti-correlation between D and M_B with $W_r(2796)$; (3) The correlation between [O II] luminosity surface density ($\Sigma L_{[\text{O II}]}$) and $W_r(2796)$; (4) The correlation between galaxy asymmetry (A), normalized by D , and $W_r(2796)$; (5) The anti-correlation between the host galaxy halo mass (M_{halo}) and $W_r(2796)$. Bouché et al. (2006) did not provided parametrized relationship for their correlation, however we used the binned data from their Table 3 and applied a least squares fit.

Properties	Redshift Range	$W_r(2796)$ Range (Å)	(Anti-) Correlation	Significance	Parametrized Relationship	Reference
i/D & $W_r(2796)$	0.3–1.0	0.03–2.9	Correlation	4.3σ	$\log(W_r(2796)) = -0.334 - 1.310\log(D/i)$	This paper.
$D + M_B$ & $W_r(2796)$	0.1–0.5	0.1–2.4	Anti-correlation	7σ	$\log(W_r(2796)) = A\log(D) - B(M_B - M_B^*) + C$ $A = -1.93 \pm 0.11$, $B = -0.27 \pm 0.02$ $C = 2.51 \pm 0.16$	Chen et al. (2010a)
$\Sigma L_{[\text{O II}]}$ & $W_r(2796)$	0.4–1.3	0.7–6.0	Correlation	15σ	$\Sigma L_{[\text{O II}]} = A(W_r(2796)/1\text{Å})^\alpha$ $A = 1.48 \pm 0.18 \times 10^{37} \text{erg s}^{-1} \text{kpc}^2$ $\alpha = 1.75 \pm 0.11$	Ménard et al. (2009)
A/D & $W_r(2796)$	0.3–1.0	0.03–2.9	Correlation	3.3σ	$A/D = 2.48 \times 10^{-3} W_r(2796) + 8.15 \times 10^{-4}$	Kacprzak et al. (2007)
M_{halo} & $W_r(2796)$	0.4–0.8	0.5–5.0	Anti-correlation	...	$\log(M_{\text{halo}}) = 13 - 0.6W_r(2796)$	Bouché et al. (2006)

Mg II absorption profiles in the lower equivalent width regime. For our sample, we find trends that weaker absorption properties are associated with redder galaxies; but there is no suggested trend directly with $W_r(2796)$ as found for higher $W_r(2796)$ systems as reported by Zibetti et al. (2007). The lack of statistical significance may be due to the small number of galaxies in our sample. For a sample of 71 absorption selected galaxies with a $W_r(2796)$ distribution similar to our sample, Chen et al. (2010a) also did not find a significant correlation between $W_r(2796)$ and galaxy color. The discrepancy between Zibetti et al. and our work and Chen et al. may indicate that there is a fundamental difference in the galaxies selected by stronger and weaker Mg II absorption systems; weaker systems are possibly not correlated with host galaxy star-formation rates or the luminosity-weighted stacking procedure is not fully understood. However, this correlation may have a substantial scatter, so that large samples, on the order of those used by Zibetti et al., are required to obtain statistical significance.

The Mg II equivalent widths, and the other measures of the Mg II column density, decrease with D , indicating that halos exhibit a natural decrease in gas column density with increasing projected galactocentric distance. This anti-correlation alone cannot be leveraged to differentiate between wind scenarios and other Mg II gas producing mechanisms; however, we would expect a difference in the halo gas geometry for the competing scenarios (see § 3.6 and § 3.7). Our sample exhibits trends for increasing absorption properties (and scatter) with higher inclination galaxies. Accounting for the decreasing gas column density (and its scatter) with increasing D reduces the scatter and yields a strong correlation (4.3σ). At the very least, this suggests that the combined effect of inclination and impact parameter is such that weaker absorption is found at larger D and smaller i (far from face-on galaxies). As i increases for a given D , we see $W_r(2796)$ increases, or as D decreases for a given i , we see $W_r(2796)$ increases. Given that the velocity widths, W_{vs} , do not follow this behavior, the data favor an increasing column density (path length) for increasing inclination at a fixed D . Such behavior is expected for co-planer geometry with kinematics that are not strictly coupled to disk rotation, but is not what is expected for a wind geometry. For a simple wind scenario, an anti-correlation between $W_r(2796)$ and i/D would be expected. These trends are not evident in our data.

Recent cosmological SPH simulations of Stewart et al. (2011)

have shown that gas-rich mergers and cold-flow streams can produce a circum-galactic cool gas component that predominately infalls towards the host galaxy disk. They note that this gas accretion should be observed as a relative host-galaxy/halo-gas velocity offsets of $\sim 100 \text{ km s}^{-1}$. These offsets have already been directly observed at $z \sim 0.1 - 1.0$ using Mg II absorption systems (Steidel et al. 2002; Kacprzak et al. 2010a, 2011). In such a scenario one would expect a correlation between host galaxy inclination and absorption strength, column density, etc., if the circum-galactic component was a pure extension of the host galaxy disk. According to these simulations, Stewart et al. (2011) found that in most cases the accreting gas co-rotates with the central disk in the form of a warped extended cold flow disk, and the observed velocity offset are in the same direction as galaxy rotation. These models support the correlations between the absorption properties and i/D found here, and the warps observed in the simulations may further explain the scatter seen in these correlations.

The relative gas–galaxy kinematics also differ between low and high equivalent width systems. Bond et al. (2001b) studied the kinematics $W_r(2796) > 1.8 \text{ Å}$ systems and found characteristics of wind driven gas (double quasi-symmetric absorption over $\sim 400 \text{ km s}^{-1}$, not characteristic of Mg II in DLAs). On the other hand, systems with $W_r(2796) \leq 1 \text{ Å}$ are characterized by velocity widths no greater than $\sim 50 \text{ km s}^{-1}$ accompanied by one to a few very weak and narrow components and are not suggestive of wind kinematics (Churchill & Vogt 2001; Churchill, Vogt, & Charlton 2001). For predominantly $W_r(2796) \leq 1 \text{ Å}$ systems, Chen et al. (2010a) found that the velocity differences between the Mg II absorption and the host galaxies are roughly 16 km s^{-1} with a dispersion of 137 km s^{-1} . These velocity offsets are much lower than expected for wind driven outflows.

In fact, a direct kinematic comparison of six galaxies and their Mg II absorption kinematics, with velocity offsets similar to those of Chen et al., were shown to be fairly well described as having lagging disk-like kinematics, though not all of the velocity spread could be successfully modeled (Steidel et al. 2002). However, the discrepancies were on the order of 30 km s^{-1} in the most extreme cases. For a similar sample, Kacprzak et al. (2010a) also showed that, even if the Mg II absorption tends to reside fully to one side of the galaxy systemic velocity and aligns with one arm of the rotation curve, not all the absorbing gas kinematics can be explained

by a co-rotating halo model. Using cosmological simulations, they further showed that even if the majority of the simulated MgII absorption arises is an array of structures, such as filaments and tidal streams, the halo gas often has velocities consistent with the galaxy rotation velocity. The line of sight gas motions along these structures in the simulations reproduce a velocity distribution consistent with that reported by Chen et al. (2010a).

Finally, it is also interesting to note the equivalent width redshift path density evolution of MgII absorbers: higher equivalent width systems evolve in that there are fewer high $W_r(2796)$ systems per unit redshift at low redshifts than at higher redshifts. The evolution is more pronounced for the highest $W_r(2796)$ systems, i.e., those with 2 \AA and above. As lower $W_r(2796)$ systems are examined, the evolution weakens such that for all systems with $W_r(2796) > 0.3 \text{ \AA}$ the absorber population is consistent with the no-evolution expectation for the presently accepted cosmology (Steidel & Sargent 1992; Nestor et al. 2005). Assuming winds are a transient phenomenon in most galaxies, and given that the global star formation rate of the universe decreases toward low redshifts (Madau et al. 1998), it would seem reasonable that, globally, the higher equivalent width systems have some causal connection to star formation rates. On the other hand, the fact that lower equivalent width systems do not evolve with redshift would indicate that the processes producing lower $W_r(2796)$, though varied, are fairly constant with cosmic time. Though major merger rates are expected to decrease strongly, $\propto (1+z)^{2.1}$, with redshift (cf., Stewart et al. 2009), it is not clear that other scenarios such as minor mergers and/or accretion of the IGM (filaments, etc.) evolve as rapidly. It could be that the lack of redshift evolution of lower $W_r(2796)$ absorbers is linked to the latter, possibly more ubiquitous processes.

The different physical characteristics and evolution of the populations of high and low $W_r(2796)$ MgII systems suggest different physical mechanisms giving rise to each population. The correlation between $W_r(2796)$ and i/D for our lower $W_r(2796)$ sample indicates that winds do not dominate the lower equivalent width regime. It appears that galaxy inclination plays a strong role in determining the optical depth of the halo gas once the decreasing column density with increasing impact parameters is taken into account. We find that edge-on systems are likely to produce higher optical depth absorption systems, and lower optical depth absorption systems are produced by face-on galaxies: this is the opposite effect expected for a wind scenario. These results support a picture where the MgII absorption arises in structures that are relatively co-planar to the host galaxy disk. Such structures might include accreting filaments or tidal streams from minor mergers in the galaxy plane, and disk warps. These results are consistent with recent cosmological simulations of Stewart et al. (2011) who find that the accretion of cool gas via filaments and gas rich merges does in fact form a stable disk that supplies gas and angular momentum to the host galaxy.

5 CONCLUSIONS

We have performed a detailed study of a sample of 40 MgII absorption-selected galaxies between $0.3 < z < 1.0$. The galaxies have B-band absolute magnitudes that range between $-18.6 \leq M_B \leq -23.8$ and are associated with MgII absorption systems with rest-frame equivalent widths that range between $0.03 \leq W_r(2796) \leq 2.9 \text{ \AA}$. The MgII absorption profiles were obtained from HIRES/Keck and UVES/VLT quasar spectra; we did not have high resolution spectra for six systems and use equivalent width

measurements from the literature. The galaxies are at projected separations of $12 \leq D \leq 115 \text{ kpc}$ from the quasar line-of-sight.

We have used GIM2D to model WFPC-2/HST images and extract quantified morphological parameters for 40 MgII absorption-selected galaxies. These parameters include: the bulge-to-total fraction (B/T), the bulge semi-major axis effective radius (r_b), the bulge ellipticity (e_b), the bulge position angle (θ_b), the bulge Sérsic index (n), the semi-major axis disk scale length (r_d), the disk inclination (i), and the disk position angle (θ_d). These properties help us further compare and quantify the nature of absorption-selected galaxies.

Furthermore, we have extracted absorption parameters from the quasar spectra as well as from Voigt profiles fits to the absorption systems. We have measured the optical depth weighted mean MgII $\lambda 2796$ absorption redshift, the rest-frame equivalent width $W_r(2796)$, the doublet ratio, the number of clouds, the Voigt profile fitted system column density, the MgII optical depth, the AOD derived column density, the mean velocity, the velocity spread, and the velocity asymmetry.

In order to explore possible connections between the MgII absorption properties and the galaxy morphological properties, we have performed non-parametric Spearman and Kendall rank correlation tests. Our main results can be summarized as follows:

(i) MgII host galaxies appear to be similar to those at low redshift and have a wide range of morphologies and colors. With 27 late-type galaxies and 13 early-type galaxies, their populations are consistent with the distribution of galaxy morphologies found in the field environment. They have a mean disk scale length of 3.8 kpc and a mean bulge scale length 2.5 kpc , which are comparable those of the Milky Way. The disk scale lengths and bulge effective radii distributions of the sample are similar to those of field galaxies obtained from the DEEP survey, at similar redshifts. The mean $W_r(2796)$ for the early-type galaxies is 1.0 \AA and slightly lower for late-type galaxies at 0.7 \AA , where both types have a large spread in equivalent width, although late-type galaxies dominate for absorption systems with $W_r(2796) < 0.3 \text{ \AA}$ and tend to also be at $D > 40 \text{ kpc}$.

(ii) We find a 3.2σ anti-correlation between D and MgII equivalent width. There is large a scatter in the distribution, suggesting that D is not the only physical parameter affecting the distribution and quantity of halo gas. There are no other absorption properties that scale with D above 3σ . However, *all* our other measures of the gas absorption strength show decreasing trends with D . Taken together, the anti-correlation trends show a consistent signature that, on average, MgII absorbing gas becomes optically thinner with increasing projected galactocentric distance from the host galaxy and is likely the dominant behavior of the halo gas.

(iii) We find only weakly significant trends ($2 - 2.2\sigma$) between color and the absorption properties, suggesting that larger absorption quantities tend to be associated with the bluer galaxies. We do not reproduce the $B - K$ and $W_r(2796)$ correlation of Zibetti et al. (2007). Our results are consistent with Chen et al. (2010a) and we conclude that our samples probe a lower equivalent width range than Zibetti et al., and therefore are likely probing different mechanisms producing MgII absorption. We find less than a 1σ connection between M_B and the absorption properties, implying that for our luminosity and equivalent width range the MgII absorption is not strongly dependent on galaxy luminosity.

(iv) We find no correlation between θ and the absorption properties (the highest significance is 1.4σ); the absorption properties

are consistent with a random distribution as a function of position angle.

(v) By accounting for the decreasing gas column density (and its scatter) with increasing D , the correlation with i/D and $W_r(2796)$ increases to 4.3σ significance level. Also, following normalization of i by D , we find that N_a , τ , N_{cl} , N_{vp} and $W_r(2803)$ are all correlated with i/D greater than 3.2σ level of significance. Overall, these results suggest that the MgII gas has co-planer geometry, but is not necessarily disk-like, that is coupled to the galaxy inclination. This results do not support MgII absorption produce by star-burst driven winds. These results are consistent with the models of Stewart et al. (2011).

(vi) We do not find any other correlations above 2.0σ between the remaining galaxy properties, such as r_b , r_h , r_e , B/T , n and the absorption properties. Thus, the galaxy optical size and shape does not appear to be an important factor in determining the amount of gas within a galaxy halo.

We find several interesting connections between the galaxy morphological properties and the MgII absorbing gas. Although recent evidence suggests that high equivalent width systems are produced predominantly by winds in star-forming galaxies, the results of this paper do not support such an explanation for weaker systems ($W_r(2796) \lesssim 1 \text{ \AA}$). The correlation between the inclination of the galaxy disk and the halo gas absorption strength suggests that the halo gas resides in a co-planer distribution. It is plausible that the absorbing gas arises from tidal streams, satellites, filaments, etc. which tend to have more-or-less co-planer distributions. This correlation could not be explained in the wind scenario.

One of the few ways to differentiate between winds and other sources replenishing the halo gas is by studying multi-phase gas sensitive to different density and temperatures. These questions express the necessity of UV spectrographs like COS and STIS.

ACKNOWLEDGMENTS

We thank Simon Mutch for his contributions to the manuscript. We also thank Nicolas Bouché and Simon Lilly for careful reading manuscript and providing comments. We thank the anonymous referee for providing insightful comments and improving the paper. M.T.M thanks the Australian Research Council for a QEII Research Fellowship (DP0877998). CWC and JLE were partially supported by the National Science Foundation under Grant Number AST-0708210. This work is based in part on observations made with the NASA/ESA *Hubble Space Telescope*, or obtained from the data archive at the Space Telescope Institute (STScI), which is a collaboration between STScI/NASA, the Space Telescope European Coordinating Facility (ST-ECF/ESA) and the Canadian Astronomy Data Centre (CAD/C/NRC/CSA). Other observations were obtained with the European Southern Observatory (ESO) Very Large Telescope at the Paranal Observatories and with the W.M. Keck Observatory (some of which were generously provided by Jason X. Prochaska and by Wallace L. W. Sargent and Michael Rauch), which is operated as a scientific partnership among the California Institute of Technology, the University of California and the National Aeronautics and Space Administration. Keck Observatory was made possible by the generous financial support of the W.M. Keck Foundation.

REFERENCES

- Barton, E. J., & Cooke, J. 2009, *AJ*, 138, 1817
- Bergeron, J., & Boissé, P. 1991, *A&A*, 243, 334
- Bond, N. A., Churchill, C. W., Charlton, J. C., & Vogt, S. S. 2001a, *ApJ*, 557, 761
- Bond, N. A., Churchill, C. W., Charlton, J. C., & Vogt, S. S. 2001b, *ApJ*, 562, 641
- Bertin, E., & Arnouts, S. 1996, *A&AS*, 117, 393
- Boksenberg, A., & Sargent, W. L. W. 1978, *ApJ*, 220, 42
- Bouché, N., Murphy, M. T., Péroux, C., Csabai, I. & Wild, V. 2006 *MNRAS*, 371, 495
- Charlton, J. C., & Churchill, C. W. 1996, *ApJ*, 465, 631
- Chelouche, D., Ménard, B., Bowen, D. V., & Gnat, O. 2008, *ApJ*, 683, 55
- Chen, H.-W., Wild, V., Tinker, J. L., Gauthier, J.-R., Helsby, J. E., Shectman, S. A., & Thompson, I. B. 2010b, *ApJ*, 724, L176
- Chen, H.-W., Helsby, J. E., Gauthier, J.-R., Shectman, S. A., Thompson, I. B., & Tinker, J. L. 2010a, *ApJ*, 714, 1521
- Chen, H.-W., Lanzetta, K. M., Webb, J. K., & Barcons, X. 1998, *ApJ*, 498, 77
- Chen, H.-W., Lanzetta, K. M., Webb, J. K., & Barcons, X. 2001, *ApJ*, 559, 654
- Chen, H.-W. & Lanzetta, K. M. 2003, *ApJ*, 597, 706
- Chen, H.-W., & Tinker, J. L. 2008, *ApJ*, 687, 745
- Churchill, C. W. 1997, Ph.D. Thesis, University of California, Santa Cruz
- Churchill, C. W., Mellon, R. R., Charlton, J. C., Jannuzi, B. T., Kirhakos, S., Steidel, C. C., & Schneider, D. P. 2000a, *ApJS*, 130, 91
- Churchill, C. W., Mellon, R. R., Charlton, J. C., Jannuzi, B. T., Kirhakos, S., Steidel, C. C., & Schneider, D. P. 2000b, *ApJ*, 543, 577
- Churchill, C. W., Rigby, J. R., Charlton, J. C., & Vogt, S. S. 1999, *ApJS*, 120, 51
- Churchill, C. W., Steidel, C. C., & Vogt, S. S. 1996, *ApJ*, 471, 164
- Churchill, C. W., & Vogt, S. S. 2001, *AJ*, 122, 679
- Churchill, C. W., Vogt, S. S., & Charlton, J. C. 2003, *AJ*, 125, 98
- Dekker, H., D'Odorico, S., Kaufer, A., Delabre, B., & Kotzlowski H. 2000, *SPIE*, 4008, 534
- Ellingson, E., Green, R. F., & Yee, H. K. C. 1991, *ApJ*, 378, 476
- Ellison, S. L., Mallén-Ornelas, G., & Sawicki, M. 2003, *ApJ*, 589, 709
- Faber, S. M., et al. 2007, *ApJ*, 665, 265
- Feigelson, E. D., & Nelson, P. I. 1985, *ApJ*, 293, 192
- Foltz, C. B., Weymann, R. J., Peterson, B. M., Sun, L., Malkan, M. A., & Chaffee, F. H., Jr. 1986, *ApJ*, 307, 504
- Gauthier, J.-R., Chen, H.-W., & Tinker, J. L. 2009, *ApJ*, 702, 50
- Guillemin p., & Bergeron, J. 1997, *A&A*, 328, 499
- Hammer, F., Flores, H., Puech, M., Yang, Y. B., Athanassoula, E., Rodríguez, M., & Delgado, R. 2009, *A&A*, 507, 1313
- Hammer, F., Flores, H., Elbaz, D., Zheng, X. Z., Liang, Y. C., & Cesarsky, C. 2005, *A&A*, 430, 115
- Hammer, F., Puech, M., Chemin, L., Flores, H., & Lehnert, M. D. 2007, *ApJ*, 662, 322
- Kacprzak, G. G., Churchill, C. W., Barton, E. J., & Cooke, J. 2011, *arXiv:1102.4339*
- Kacprzak, G. G., Churchill, C. W., Steidel, C. C., & Murphy, M. T. 2008, *AJ*, 135, 922
- Kacprzak, G. G., Churchill, C. W., Steidel, C. C., Murphy, M. T., & Evans, J. L. 2007, *ApJ*, 662, 909
- Kacprzak, G. G., Churchill, C. W., Ceverino, D., Steidel, C. C., Klypin, A., & Murphy, M. T. 2010a, *ApJ*, 711, 533
- Kacprzak, G. G., Murphy, M. T., & Churchill, C. W. 2010b, *MNRAS*, 406, 445
- Kanekar, N., & Chengalur, J. N. 2001, *MNRAS*, 325, 631
- Kinney, A. L., Calzetti, D., Bohlin, R. C., McQuade, K., Storchi-Bergmann, T. & Schmitt, H. R. 1996, *ApJ*, 467, 38
- Krist, J. & Hook, R. 2004, *The Tiny Tim User Manual v6.3* (Baltimore: STScI)
- Lanzetta, K. M., & Bowen, D. 1990, *ApJ*, 357, 321
- Lanzetta, K. M. & Bowen, D. V. 1992, *ApJ*, 391, 48L
- Lowenthal, J. D., Caulet, A., Green, R. F., Hogan, C. J., Brown, L. W., Oliversen, R. J., & Woodgate, B. E. 1990, *BAAS*, 22, 805
- Lundgren, B. F., et al. 2009, *ApJ*, 698, 819
- Madau, P., Pozzetti, L., & Dickinson, M. 1998, *ApJ*, 498, 106

- Martin, C. L., & Bouché, N. 2009, *ApJ*, 703, 1394
- Ménard, B., Wild, V., Nestor, D., Quider, A., & Zibetti, S. 2009, arXiv:0912.3263
- Metropolis, N., Rosenbluth, A. W., Rosenbluth, M. N., Teller, A. H., & Teller, E. 1953, *J. Chem. Phys.*, 21, 1087
- Miller, J. S., Goodrich, R. W., & Stephens, S. A. 1987, *AJ*, 94, 633
- Mo, H. J., & Miralda-Escude, J. 1996, *ApJ*, 469, 589
- Nestor, D. B., Johnson, B. D., Wild, V., Ménard, B., Turnshek, D. A., Rao, S., & Pettini, M. 2010, arXiv:1003.0693
- Nestor, D. B., Turnshek, D. A., & Rao, S. M. 2005, *ApJ*, 628, 637
- Nestor, D. B., Turnshek, D. A., Rao, S. M., & Quider, A. M. 2007, *ApJ*, 658, 185
- Noterdaeme, P., Srianand, R., & Mohan, V. 2010, *MNRAS*, 403, 906
- Prochter, G. E., Prochaska, J. X., & Burles, S. M. 2006, *ApJ*, 639, 766
- Rich, R. M. 1998, *The Central Regions of the Galaxy and Galaxies*, 184, 11
- Rigby, J. R., Charlton, J. C., & Churchill, C. W. 2002, *ApJ*, 565, 743
- Rubin, K. H. R., Weiner, B. J., Koo, D. C., Martin, C. L., Prochaska, J. X., Coil, A. L., & Newman, J. A. 2009, arXiv:0912.2343
- Saha, P., & Williams, T. B. 1994, *AJ*, 107, 1295
- Schneider, D. P., et al. 1993, *ApJS*, 87, 45
- Sérsic, J. L. 1968, *Cordoba, Argentina: Observatorio Astronomico*
- Simard, L., Willmer, C. N. A., Vogt, N. P., Sarajedini, V. L., Philips, A. C., Weiner, B. J., Koo, D. C., Im, M., Illingworth, G. D., & Faber, S. M. 2002, *ApJS*, 142, 1
- Steidel, C. C. 1995, in *QSO Absorption Lines*, ed. G. Meylan, (Springer-verlag: Berlin Heidelberg), p. 139
- Steidel, C. C. 1998, in *Galactic Halos: A UC Santa Cruz Workshop*, ed. D. Zaritsky, ASP Conference Proceeding, V136, p167
- Steidel, C. C., Dickinson, M., Meyer, D. M., Adelberger, K. L., & Sembach, K. R. 1997, *ApJ*, 480, 586
- Steidel, C. C., Dickinson, M., & Persson, S. E. 1994, *ApJ*, 437, L75
- Steidel, C. C., Erb, D. K., Shapley, A. E., Pettini, M., Reddy, N., Bogosavljević, M., Rudie, G. C., & Rakic, O. 2010, *ApJ*, 717, 289
- Steidel, C. C., Kollmeier, J. A., Shapely, A. E., Churchill, C. W., Dickinson, M., & Pettini, M. 2002, *ApJ*, 570, 526
- Steidel, C. C., & Sargent, W. L. W. 1992, *ApJS*, 80, 1
- Stewart, K. R., Kaufmann, T., Bullock, J. S., Barton, E. J., Maller, A. H., Diemand, J., & Wadsley, J. 2011, arXiv:1103.4388
- Stewart, K. R., Bullock, J. S., Barton, E. J., & Wechsler, R. H. 2009, *ApJ*, 702, 1005
- Tremonti, C. A., Moustakas, J., & Diamond-Stanic, A. M. 2007, *ApJl*, 663, L77
- Tripp, T. M., & Bowen, D. V. 2005, in *Probing Galaxies through Quasar Absorption Lines*, IAU 199 Proceedings, eds. P. R. Williams, C.-G. Shu, & B. Ménard (Cambridge: Cambridge University Press), p. 5
- van den Bergh, S. 2004, *AJ*, 128, 1138
- Veilleux, S., Cecil, G., & Bland-Hawthorn, J. 2005, *ARA&A*, 43, 769
- Vogt, N. P., et al. 2005, *ApJS*, 159, 41
- Vogt, S. S., et al. 1994, *SPIE*, 2198, 362
- Weiner, B. J., et al. 2009, *ApJ*, 692, 187
- Weiner, B. J., et al. 2005, *ApJ*, 620, 595
- Weinzirl, T., Jogee, S., Khochfar, S., Burkert, A., & Kormendy, J. 2009, *ApJ*, 696, 411
- Whitmore B., 1995, *Photometry with the WFPC2*. In: Koratkar A., Litherer C. (eds.) *Calibrating Hubble Space Telescope: Post servicing mission*, STScI, Baltimore
- Zibetti, S., Ménard, B., Nestor, D. B., Quider, A. M., Rao, S. M., & Turnshek, D. A. 2007, *ApJ*, 658, 161

APPENDIX A: APPENDIX A: SUPPORTING INFORMATION

Figure A1 is the complete version of Figure 1. It will appear in the online version of this paper, not in the printed version.

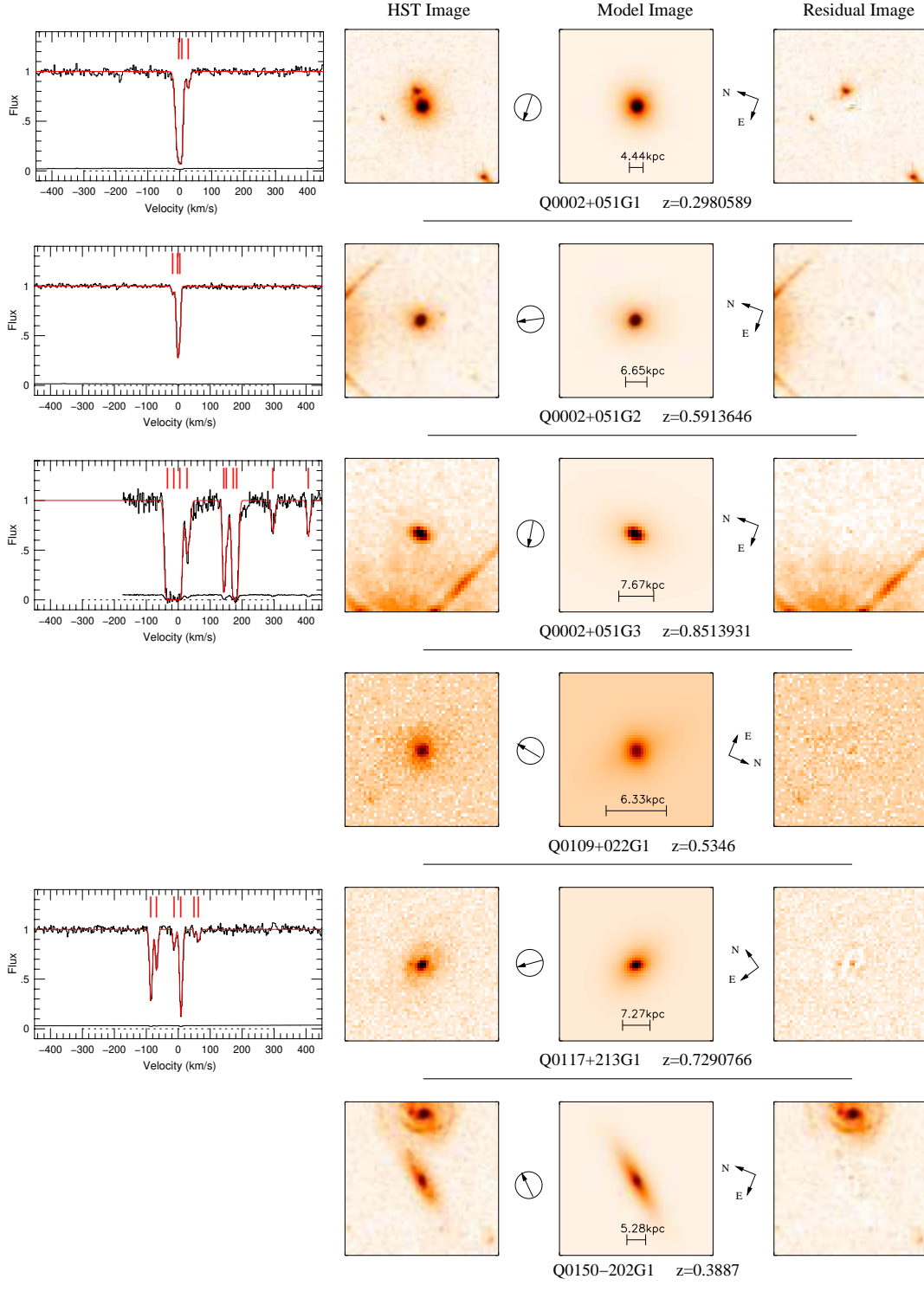


Figure A1. — (far-left) The Hires/Keck or UVES/VLT quasar spectra of the Mg II $\lambda 2796$ absorption feature are shown alongside the associated absorbing galaxy on the right. The Mg II $\lambda 2796$ optical depth weight mean absorption redshift is the zeropoint of the velocity scale. The tick marks indicate the number of Voigt profile components and the red curve indicates the fit to the data. We do not have Hires or UVES data available for six galaxies. (left) WFPC-2/*HST* images of galaxies selected by Mg II absorption. The images are 10 times larger than the 1.5σ isophotal area. — (center) The GIM2D models of the galaxies, which provide quantified morphological parameters. A scale of one arcsecond is indicated on each image along with the physical scale computed at the Mg II absorption redshift. — (right) The residual images from the models, showing quality of the fit and the underlying structure and morphological perturbations of the galaxies. The encircled arrow provides the direction to the quasar (galaxy-quasar orientation). The cardinal directions are also shown and the quasar name and redshift of Mg II absorption is provided under each set of galaxy WFPC-2, model and residual image.

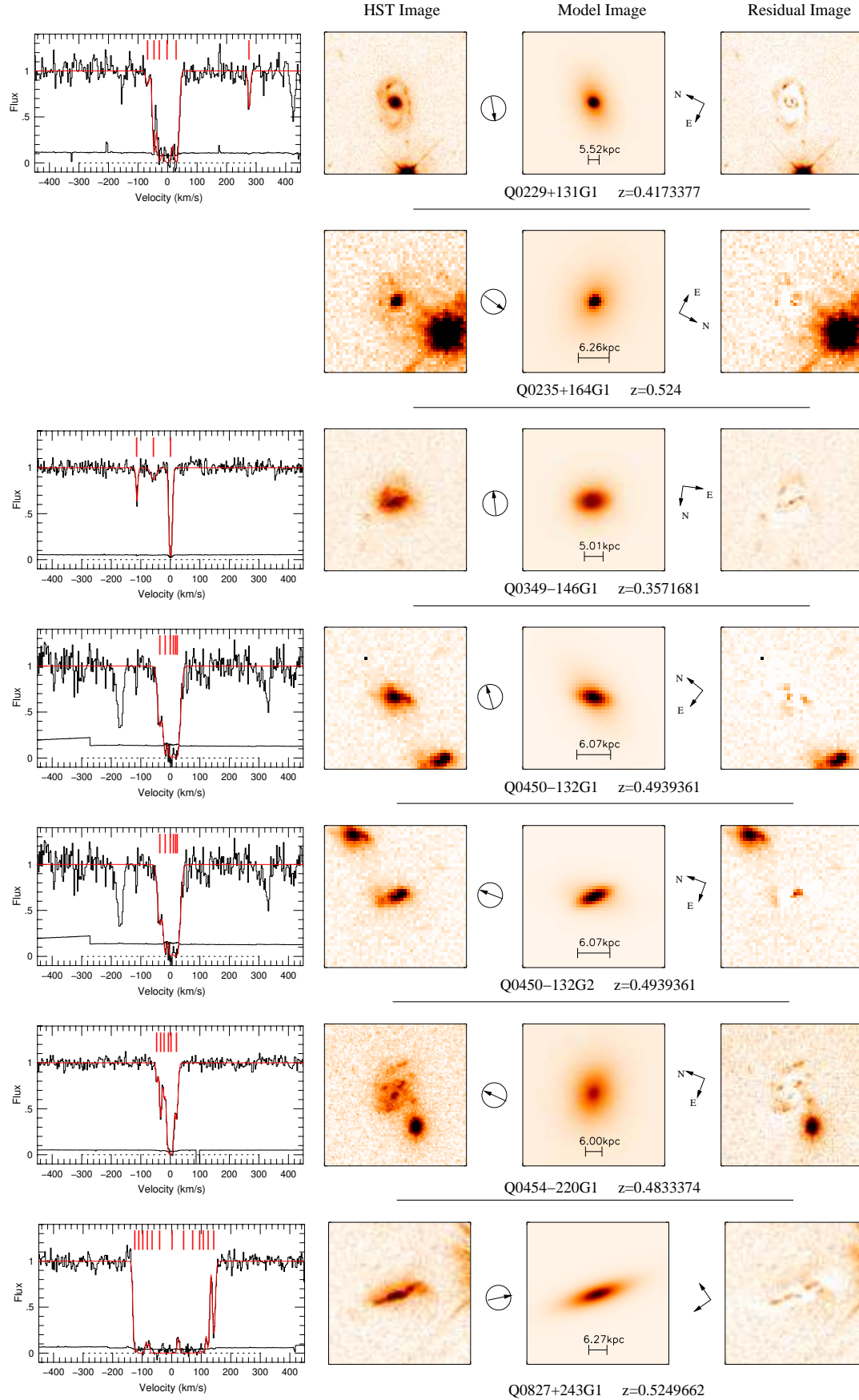


Figure A1. — continued

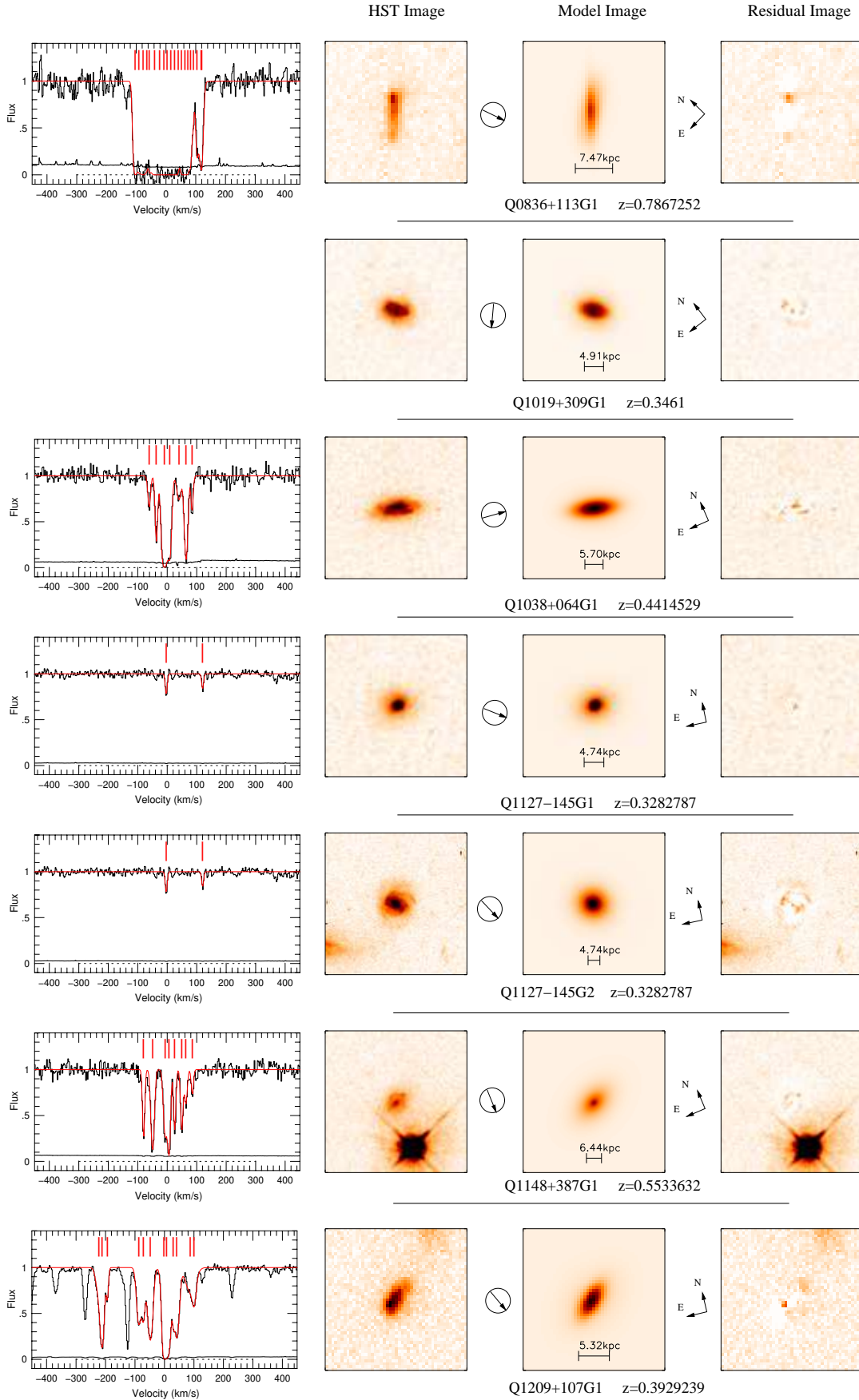


Figure A1. — continued

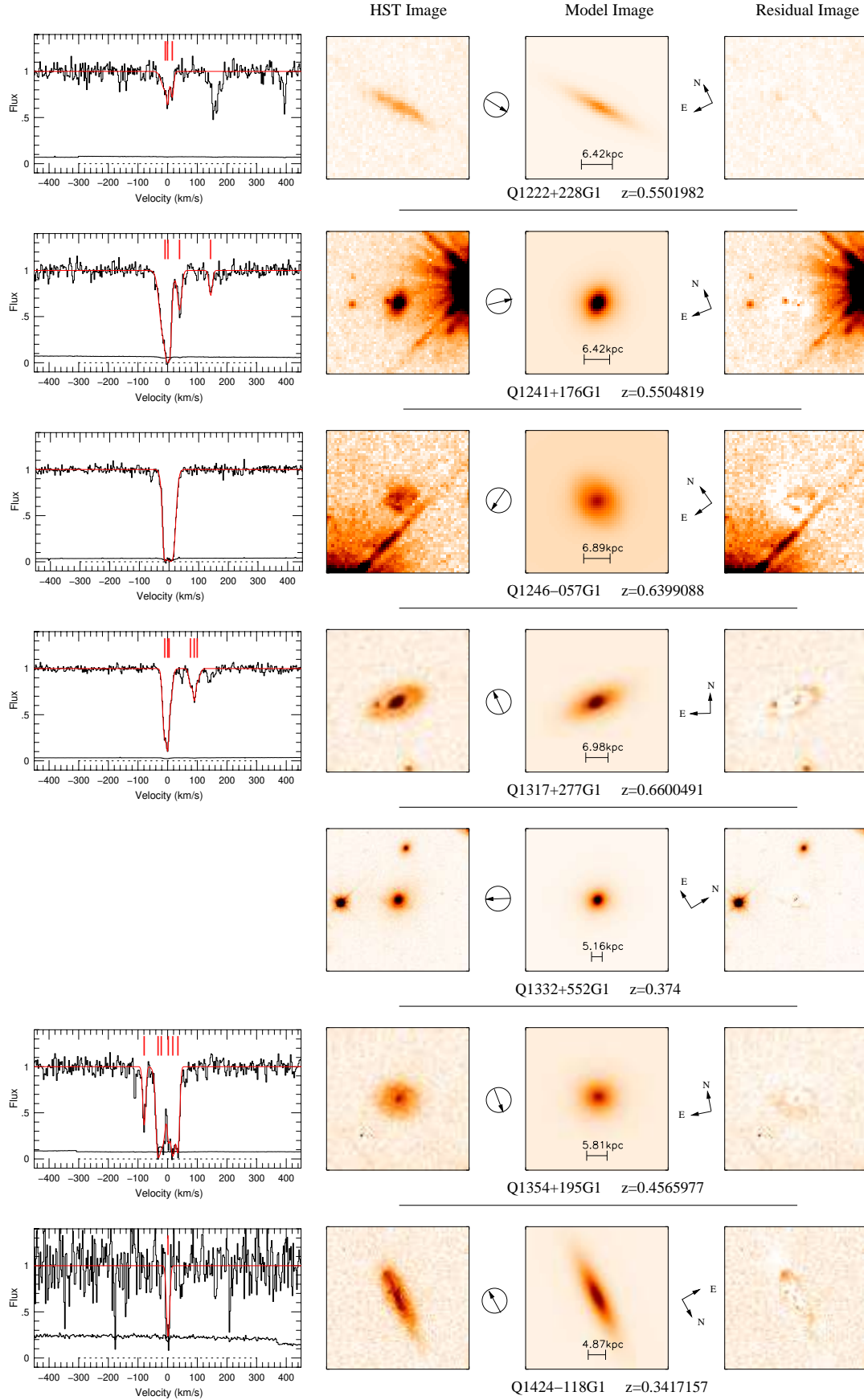


Figure A1. — continued

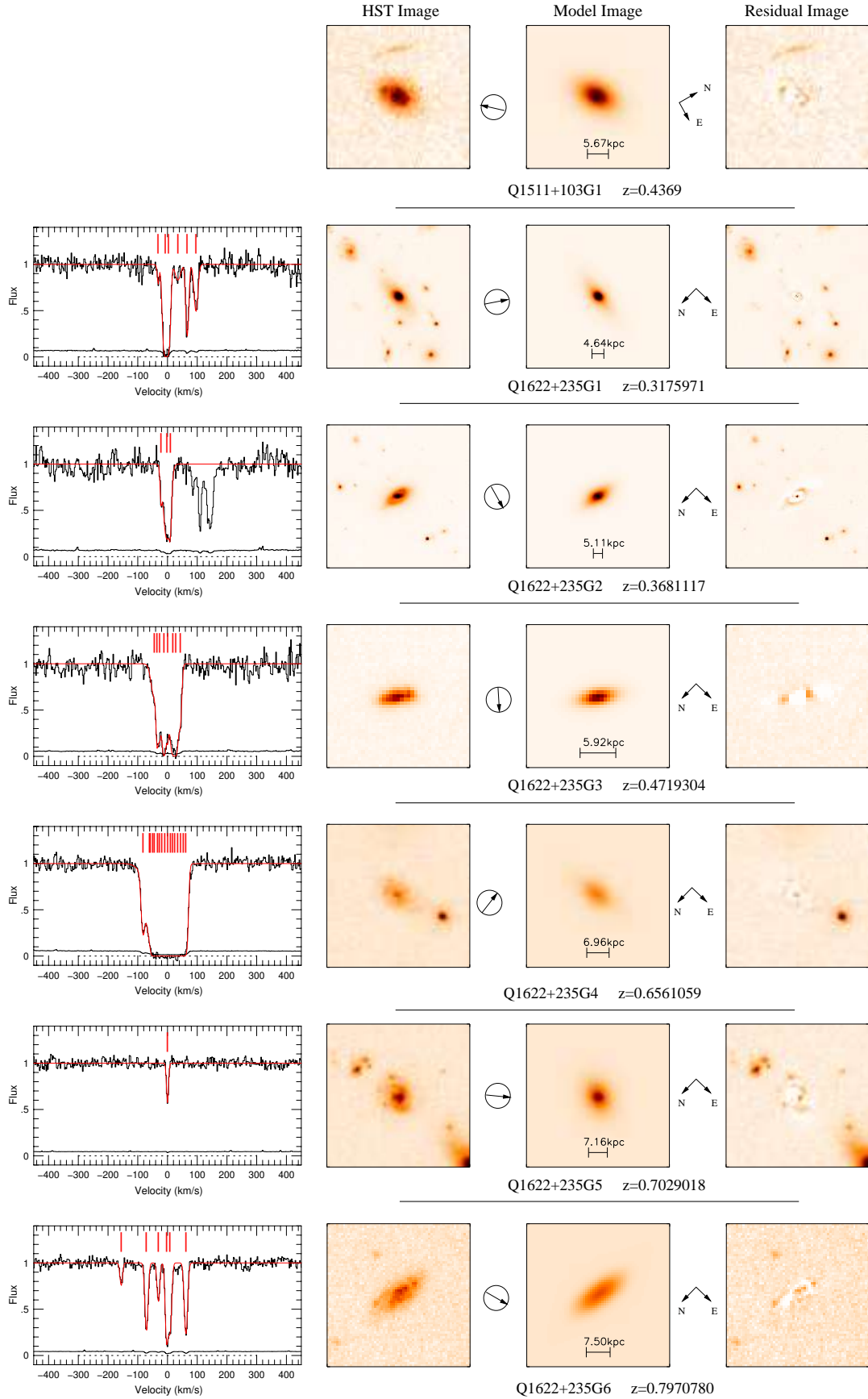


Figure A1. — continued

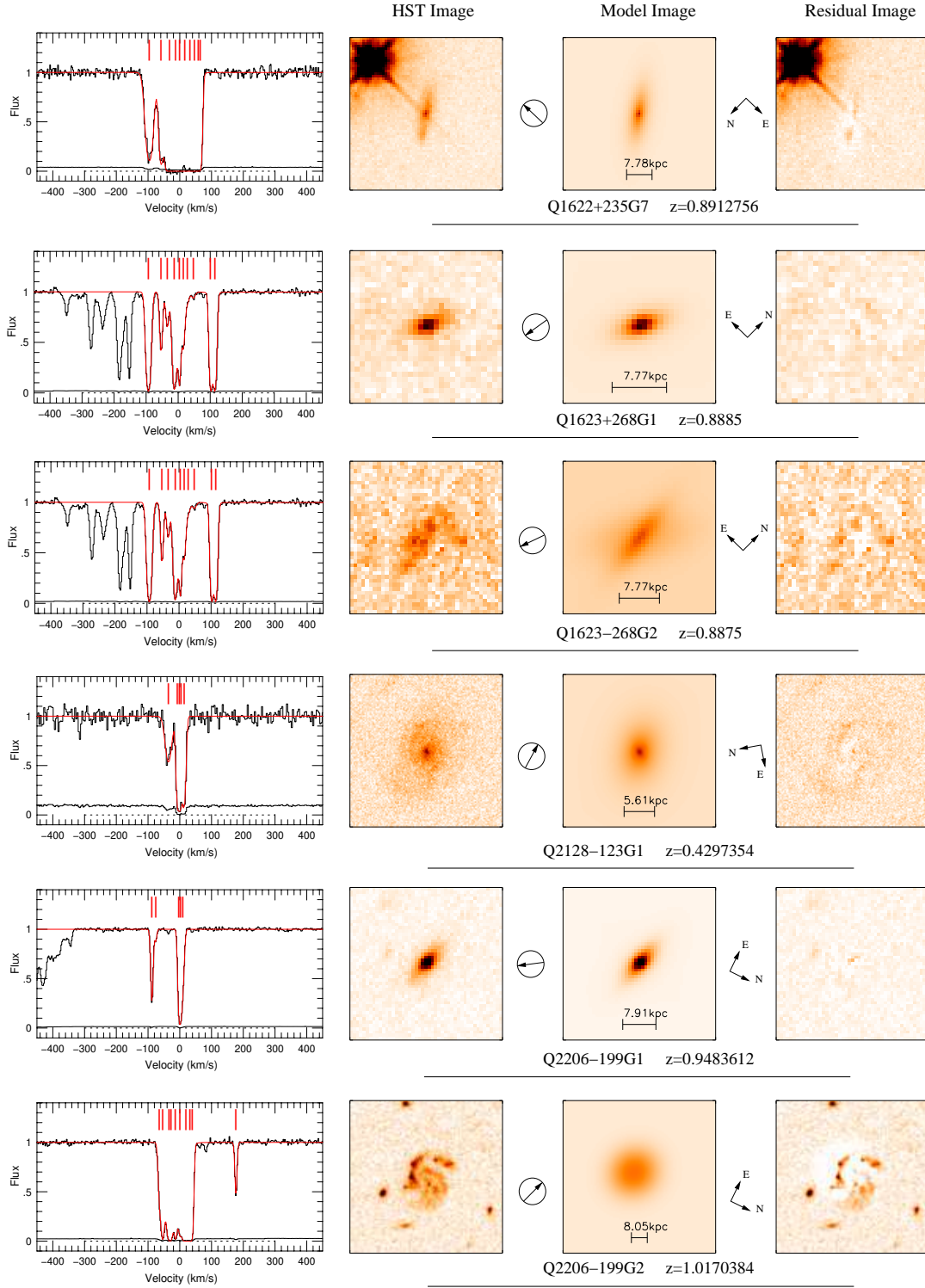


Figure A1. — continued